

# Vortex-Free Intrinsic Orbital Angular Momentum

WENXIANG YAN,<sup>1,2,†</sup> ZHENG YUAN,<sup>1,2,†</sup> YUAN GAO,<sup>1,2</sup> XIAN LONG,<sup>1,2</sup> ZHI-CHENG REN,<sup>1,2</sup> XI-LIN WANG,<sup>1,2</sup> JIANPING DING,<sup>1,2,3,\*</sup> AND HUI-TIAN WANG,<sup>1,2,4</sup>

<sup>1</sup> National Laboratory of Solid State Microstructures and School of Physics, Nanjing University, Nanjing 210093, China

<sup>2</sup> Collaborative Innovation Center of Advanced Microstructures, Nanjing University, Nanjing 210093, China

<sup>3</sup> Collaborative Innovation Center of Solid-State Lighting and Energy-Saving Electronics, Nanjing University, Nanjing 210093, China

<sup>4</sup> htwang@nju.edu.cn

<sup>†</sup>These authors contributed equally to this work.

\*jpding@nju.edu.cn

## Abstract

For three decades, optical orbital angular momentum (OAM) has been synonymous with phase vortices. Here, our research challenges this paradigm by demonstrating a vortex-free intrinsic OAM arising from three-dimensional caustic trajectories in structured light fields, distinct from traditional vortex-based mechanisms. Optical OAM was traditionally considered rare, predominantly manifesting during high-order atomic and molecular transitions. The conceptual shift initiated by Allen et al. in 1992, which showed that laser beams with optical vortex—characterized by their twisted wavefronts—naturally carry intrinsic OAM, laid the groundwork for subsequent studies. However, the exploration of intrinsic OAM in vortex-free laser modes remains a largely untapped area. Addressing this gap, our research proposes a third category of optical intrinsic angular momentum—termed "vortex-free OAM"—that complements spin angular momentum (SAM) in circularly polarized beams and OAM in vortex beams. This new form of OAM is governed by a hydrodynamic analogy between light propagation and fluid dynamics, linking the orbital motion of energy streamlines to quantifiable angular momentum. Through numerical simulations, experimental measurements, and investigations of the mechanical transfer of OAM to trapped particles using optical tweezers, we establish vortex-free OAM as a universal property of structured fields with three-dimensional caustic trajectories. Furthermore, we propose a unified hydrodynamic framework that transcends traditional wavefront-centric models, facilitating the generalization of OAM analysis to both vortex and vortex-free regimes. This framework not only enhances our understanding of the physical origin of optical angular momentum but also unlocks new opportunities in optical manipulation, classical and quantum communications, and light-matter interaction technologies.

## Introduction

The quest to unravel light's hidden rotational dynamics began with Kepler's 17th-century insight that comet tails pointed away from the Sun implied light carries linear momentum—a conjecture later formalized as radiation pressure. This mechanical perspective reached a milestone in 1909 when Poynting<sup>1</sup> recognized that circularly polarized light inherently carries spin angular momentum (SAM) (Fig. 1D), analogous to a spinning top's rotation. Darwin<sup>2</sup> soon extended this concept, proposing that angular momentum conservation in atomic transitions necessitated another form—orbital angular momentum (OAM)—though it remained an elusive phenomenon tied to rare quantum transitions. A key development occurred when optics embraced fluid dynamical thinking: In 1989, Couillet et al.<sup>3</sup> drew a striking parallel between optical vortices and superfluid quantum vortices, revealing that laser cavities could host photon flows with whirlpool-like phase singularities. This analogy catalyzed Allen's seminal 1992 discovery<sup>4</sup>: helical wavefronts  $\exp(i\ell\phi)$  in vortex beams (Fig. 1E) endow each photon with OAM ( $\ell\hbar$ )—a value far exceeding SAM's  $\hbar$ . Suddenly, light's rotational properties became engineerable through phase vortices, enabling advancements with applications spanning optical manipulation<sup>8–10</sup>, metrology<sup>11,12</sup>, encryption<sup>13</sup>, quantum optics<sup>14,15</sup>, and optical communications<sup>16–19</sup>. Yet this very success led to predominant focus on vortex-based phenomena. Just as 19th-century

fluid dynamists fixated on whirlpools while neglecting laminar flows, the optics community focused almost exclusively on phase vortices—despite early hints of richer rotational phenomena<sup>20-22</sup>.

Despite these foundational insights, the field has remained constrained: over the past three decades, OAM research has focused almost exclusively on phase vortices—a paradigm akin to studying fluid dynamics solely through whirlpools while ignoring rivers. While pioneering work by Courtial, Dholakia, Allen, and Padgett<sup>20</sup> in 1997 explicitly noted that 'beams with other profiles can also carry OAM,' and Berry's seminal analyses<sup>21,22</sup> from 2009 to 2022 rigorously demonstrated the independence of OAM from phase vortices, the fundamental question of how angular momentum emerges in vortex-free fields has persisted as a grand challenge. This gap represents more than a missing puzzle piece—it signals a conceptual blind spot in our understanding of light's rotational dynamics, limiting applications to vortex-centric designs and overlooking vast territories of structured light.

Here, our research addresses this dichotomy through three key advances. First, by extending Poynting's mechanical analogy beyond spin angular momentum, we demonstrate a distinct intrinsic OAM in vortex-free structured light—a third category of optical intrinsic angular momentum—that complements SAM in circularly polarized beams and OAM in vortex beams (Fig. 1). This quantifiable intrinsic OAM is carried not by twisted wavefronts but by three-dimensional caustic trajectories (Fig. 1F)—termed "vortex-free OAM". These caustic trajectories function as photon 'orbital highways', where angular momentum emerges naturally from path curvature (Fig. 2), mirroring the mechanics of celestial bodies in gravitational orbits. Second, our measurements establish this new OAM form's universality through convergent evidence: (i) Numerical computation by fundamental theoretical models linking caustic geometry to quantifiable angular momentum; (ii) Precision experimental measurements via momentum-space tomography and cylindrical lens interferometry (Fig. 3); (iii) Direct mechanical transfer of OAM to microparticles in optical tweezers (Fig. 4), demonstrating the observable mechanical rotating effects. Finally, our research unifies OAM analysis through a hydrodynamic framework that transcends traditional paradigms. By mapping light's energy streamlines—the complete 'roadmap' of photon motion—our research reveals how both vortex and vortex-free OAM originate from rotational and orbital energy flows (Fig. 5). This framework not only quantifies angular momentum through measurable streamline curvature but also enables predictive design of hybrid light fields combining multiple OAM modalities (Fig. 6). Collectively, these advances redefine angular momentum as a universal property of structured light—independent of phase vortices—with potential implications spanning quantum technologies, astrophysical analogies, and photonics. By establishing hydrodynamic design principles, our framework paves the way for next-generation optical manipulation systems, high-dimensional quantum communication protocols, and biomimetic optofluidic devices.

## Result

### 1. Elucidating Intrinsic Vortex-Free OAM in Self-Accelerating Beams

#### 1.1 Photonic Orbital Motion: From Mechanical Analogy to Optical Reality

Angular momentum serves as a universal descriptor of rotational dynamics across scales—from spinning electrons to orbiting galaxies. Classical mechanics identifies three archetypal forms (Fig. 1A-C): (i) spinning particles (e.g., Earth's spin), (ii) rigid-body rotation (e.g., galactic spirals), and (iii) orbital motion (e.g., planetary orbits). In optics, two counterparts are well-established: spin angular momentum (SAM) in circularly polarized light (Fig. 1D) and vortex-based orbital angular momentum (OAM) from helical wavefronts (Fig. 1E). The third form—photon analogs of orbital motion—has remained elusive, despite its mechanical counterpart's ubiquity in celestial mechanics.

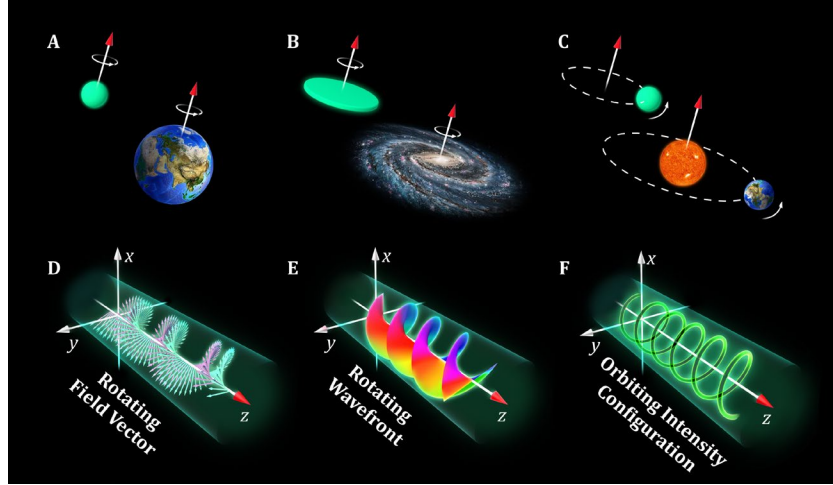


**Fig. 1.** Angular momentum models with rotational and orbital dynamics. In mechanics: (A-C) the spinning particle, rigid-body rotation, and the orbital motion of the particle, with corresponding astronomical parallels in the Earth's spin, galactic spirals, and planetary orbits (e. g. the Earth's orbit around the Sun), respectively. In optics: (D) a circularly polarized beam with rotating electric and magnetic field vectors. (E) a vortex beam with the rotating/twisted wavefront. (F) a vortex-free optical solenoid beams with the orbital intensity configuration. The red arrows depict the angular momentum.

The mechanical momentum and angular momentum of a free particle in Fig. 1C with the mass  $M$  and the orbital trajectory in a transversal plane with time  $t$  as  $\mathbf{s}(t) = x_m(t)\hat{\mathbf{x}} + y_m(t)\hat{\mathbf{y}} = r_m(t)\hat{\mathbf{r}} + \varphi_m(t)\hat{\boldsymbol{\phi}}$  are derived from its orbital trajectory and given by

$$\mathbf{p}(t) = M\mathbf{s}'(t) = M(x_m'(t)\hat{\mathbf{x}} + y_m'(t)\hat{\mathbf{y}}), \quad (1)$$

$$J_z(t) = \mathbf{s}(t) \times \mathbf{p}(t) \cdot \hat{\mathbf{z}} = M(x_m(t)y_m'(t) - y_m(t)x_m'(t)) = Mr_m^2(t)\varphi_m'(t), \quad (2)$$

where the single prime symbol denotes the first-order derivative to the variable  $t$  in parentheses and the subscript “ $m$ ” indicates “mechanical”. Analogous to the mechanical angular momentum of the orbiting free particle in Eq. 2, its optical analogue in vortex-free self-accelerating beams<sup>23–26</sup>, characterized by 3D caustic/self-accelerating trajectories along the mainlobes (e.g., the optical solenoid with a spiral trajectory shown in Fig. 1F), is explored. Defining the 3D self-accelerating caustic trajectories with propagation distance  $z$  as  $\mathbf{s}(z) = x_s(z)\hat{\mathbf{x}} + y_s(z)\hat{\mathbf{y}} = r_s(z)\hat{\mathbf{r}} + \varphi_s(z)\hat{\boldsymbol{\phi}}$ , the transversal momentum density per photon and the localized longitudinal OAM per photon along these trajectories are also quantified by their trajectories as

$$\mathbf{p}_\perp(z) = \hbar k \mathbf{s}'(z) = \hbar k(x_s'(z)\hat{\mathbf{x}} + y_s'(z)\hat{\mathbf{y}}). \quad (3)$$

$$J_{z,local}(z) = [\mathbf{s}(z) \times \mathbf{p}_\perp(z)] \cdot \hat{\mathbf{z}} = \hbar k(x_s(z)y_s'(z) - y_s(z)x_s'(z)) = \hbar k r_s^2(z)\varphi_s'(z), \quad (4)$$

where  $k$  represents the free-space wavenumber, the subscripts “ $\perp$ ” and “ $z$ ” indicates “transversal” and “longitudinal”, the single prime symbol denotes the first-order derivative to the variable  $z$  in parentheses, and the subscript “ $s$ ” indicates “self-accelerating”. The scope of this paper is concentrated on the monochromatic scalar optical fields and detailed derivations of Eqs. 3-4 are provided in the Supplementary Text 1 with Movie S1. This mechanical-optical correspondence is mathematically exact (Eqs. 1-4): the trajectory-dependent angular momentum of a free particle (Eq. 2) maps directly to the photon's OAM along 3D caustic paths (Eq. 4), differing only by the momentum scale ( $\hbar k$  vs.  $M$ ). Just as a satellite's orbit determines its angular momentum, the curvature of a photon's 'orbital highway' (Fig. 1F) dictates its OAM magnitude—a paradigm shift from vortex-based OAM's reliance on helical phase fronts. This analogy is underpinned by the correspondence between the paraxial equation in optics and the time-dependent Schrödinger equation in quantum mechanics<sup>22,27</sup>: the paraxial wave equation  $-i\partial_z\psi(x, y, z) = (\partial_x^2 + \partial_y^2)\psi(x, y, z)$  governs the paraxial propagation of waves with  $z = (\text{propagation distance})/k$ ; when  $z$  is reinterpreted as (time)  $\hbar/M$ , it aptly describes the quantum dynamics of a free particle of mass  $M$ .

Angular momentum is pivotal in analyzing systems with rotational and orbital dynamics, including optical systems. Traditional vortex beams, such as high-order Bessel beams and Laguerre-Gaussian beams, characterized by a spiral phase of  $\exp(il\phi)$ , manifest energy's rotational dynamics, initially observed by Allen et al.<sup>4</sup>, and contribute to the well-defined vortex-based OAM of  $lh$  per photon. In a broad spectrum of vortex-free structured fields<sup>20,23–26</sup>, rotational or orbital dynamics of energy are also prevalent. For instance, spirally self-accelerating Bessel-like beams<sup>24,25</sup>, shown in Fig.1F, follow the self-accelerating trajectory  $\mathbf{s}(z)=R_0[\cos(\omega_z z), \sin(\omega_z z)]$  where  $R_0$  and  $\omega_z$  denotes the spiral radius and the angular velocity with  $z$ , respectively. The transversal momentum density per photon along the orbital mainlobe, expressed as  $\hbar k \mathbf{s}'(z) = \hbar k R_0 \omega_z [-\sin(\omega_z z), \cos(\omega_z z)]$  from Eq. 3, as verified in Fig. S2G-I, mirrors the rotational energy dynamics in vortex beams<sup>4</sup>. The qualitative analysis of this new form of angular momentum along the mainlobe of spirally self-accelerating Bessel-like beams, quantified as  $\hbar k (R_0)^2 \omega_z$  by Eq. 4, aligns with the mechanical angular momentum of a uniformly orbiting particle around one point with the angular velocity  $\omega$  and the radius  $R_0$ , quantified as  $M(R_0)^2 \omega$  by Eq. 2, offering novel insights into the interplay between mechanical motion and light structure. Diverging from the traditional OAM found in vortex beams, which is characterized by rotating wavefronts, the OAM in our study, arising from the orbital caustic geometry within vortex-free structured light, is aptly termed “vortex-free OAM”. This new form of OAM, mirroring the mechanical angular momentum of orbiting free particles, expands our understanding of optical angular momentum into vortex-free fields.

## 1.2 Geometric Rendering of OAM Conservation in Structured Light.

Geometric optics<sup>28</sup> reveals why usual vortex-free structured beams lack intrinsic OAM: these photonic energy transport channels – effectively serving as photon "highways" – remain constrained either to 1D lines ( $\varphi_s(z) = 0$ ) or 2D planes ( $\varphi_s'(z) = 0$ ) (Figs. 2A-D); such dimensional limitations fundamentally prevent the emergence of the cross product term between transversal momentum and trajectory, which is essential for angular momentum (Eq. 4). The breakthrough emerges in 3D caustics (Figs. 2E-F): spiraling paths with  $\varphi_s'(z) \neq 0$  create helical momentum components (red arrows in insets of Fig. 2E), generating OAM through the same geometric mechanism as orbiting planets. This picture explains why Airy beams<sup>23</sup> (2D caustics) carry negligible OAM despite their curved trajectories ( $\varphi_s'(z) = 0$ ), while spiral caustic beams exhibit robust OAM ( $\varphi_s'(z) \neq 0$ ) by Eq. 4.

The mechanical angular momentum of an orbiting free particle is subject to variation over time  $t$ , as shown in Eq. 2. However, the total angular momentum of the entire mechanical system remains conserved. Analogously in optical systems, while the local OAM along the 3D caustic in self-accelerating beams may vary during propagation, as described by Eq. 4 with  $\hbar k r_s^2(z) \varphi_s'(z)$ , the global OAM of the optical system, represented as the average OAM density across the transverse plane, remains conserved during transmission. The geometrical mapping between transverse and longitudinal dimensions along the caustics in Bessel-like beams, depicted by the conical geometrical-optics rays in Fig. 2, ensures that the integration of energy, momentum, and OAM of all light cones across any transverse plane is equivalent to their cumulative integration along the caustic—the mainlobe constituted by the apexes of all light cones. Consequently, the global OAM per photon—the average OAM density across the transverse plane—can equate to a longitudinal average OAM density along the mainlobe, expressed as

$$\begin{aligned} J_z &= \langle I(z) J_z(z) \rangle_z / \langle I(z) \rangle_z, \\ &= \hbar k \langle I(z) r_s^2(z) \varphi_s'(z) \rangle_z / \langle I(z) \rangle_z; \end{aligned} \quad (5)$$

Similarly, the transverse net momenta<sup>29</sup>—the integration of transversal momentum density across the transverse plane, corresponds to a longitudinal integration of this momentum density along the mainlobe, expressed as

$$\mathbf{P}_\perp = \langle I(z) \mathbf{p}_\perp(z) \rangle_z = k \left( \langle I(z) x_s'(z) \rangle_z, \langle I(z) y_s'(z) \rangle_z \right), \quad (6)$$

where the shortened notation  $\langle \cdot \rangle_z = \int dz$  denotes longitudinal integration, and  $I(z)$  is the tailored intensity profile along the mainlobe, reflecting the energy-weight coefficient of OAM density per photon and transversal momentum density per

photon within the 3D caustic. Namely, the transversal momentum density or the OAM density is in proportion to the product of  $I(z)$  and the respective per-photon quantities. A detailed derivation of Eqs. 5-6 is available in the section 'OAM in Self-Accelerating Bessel-like Beams' of Supplementary Text 1. For clarity, the intensity profile along the mainlobe is considered uniformly in the main text, with setting  $I(z) = 1$ . In theory, self-accelerating Bessel-like beams, similar to ideal Bessel and Airy beams<sup>23</sup>, necessitate infinite power and aperture to sustain their non-diffracting nature over an unbounded propagation range,  $z \in (-\infty, \infty)$ . Finite physical apertures would confine these beams to a specific and manageable propagation range,  $z \in (a, b)$ . Consequently, the expressions on the left-hand sides of Eqs. 5-6 represent the global OAM and the transverse net momenta within the physical aperture and those on the right-hand sides demonstrate the integrals along the  $z$ -direction over the effective propagation distance of the beam within  $z \in (a, b)$ . This configuration, originating from the geometrical mapping relationship between the transverse and longitudinal dimensions, mirrors the interaction between the illuminating aperture of an axicon and its diffraction-free range. This modeling encapsulates the overall conservation of angular momentum despite the localized variations of angular momentum along the mainlobes, due to the vortex-free beam's dynamic propagation characteristics.

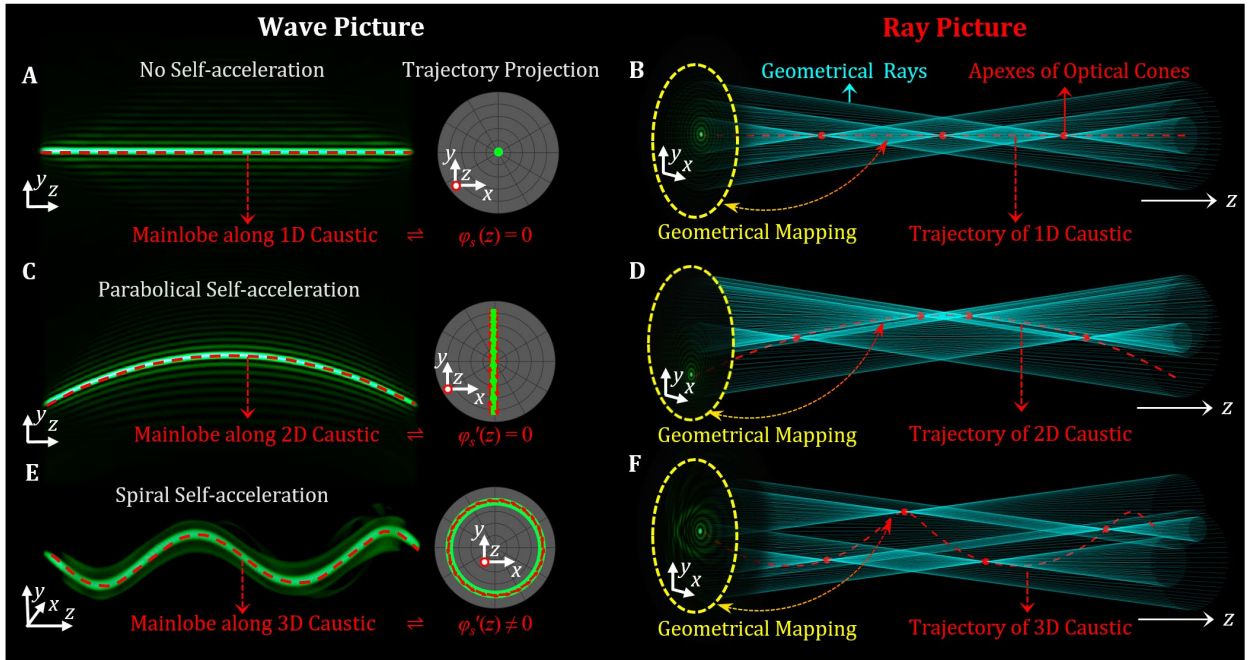


**Fig. 2.** Wave and ray pictures of self-accelerating Bessel-like beams. Subgraphs (A-B) feature that the geometrical-optics rays (the cyan lines) of 0-order Bessel beams are lying on coaxial conical surfaces and the caustic (the red-dotted line, acting as orbital highways for photons)—the straight line (i.e., the mainlobe) constituted by the apexes (the red dots) of optical cones, is termed one-dimensional (1D) caustic. Subgraphs (C-D) feature that the geometrical-optics rays (the cyan lines) of the parabolically self-accelerating Bessel-like beams<sup>24</sup> (like parabolic Airy beams<sup>23</sup>) are lying on translational conical surfaces and the parabolic caustic (the red-dotted curve) along the self-accelerating mainlobe, constituted by the apexes (the red dots) of translational light cones, is confined solely to a meridional plane that includes the  $z$  axis, referred to as two-dimensional (2D) caustic. Subgraph (E-F) feature that the geometrical-optics rays (the cyan lines) of the spirally self-accelerating Bessel-like beams (e.g., optical solenoid beams herein) are lying on translational conical surfaces and the spiral caustic (the red-dotted curve) along the self-accelerating mainlobe, constituted by the apexes (the red dots) of translational light cones, is termed 3D caustic. The yellow-dashed circles with yellow-red arrows in (B), (D), and (F) indicates geometrical mapping relationship between the transverse and longitudinal dimensions along the caustics that the integration of energy, momentum, and OAM of all light cones across any transverse plane are equivalent to the integration of those quantities along the caustic—the mainlobe constituted by the apexes of all light cones. The insets in the right of (A, C, E) depict 3D trajectory projection onto the  $x$ - $y$  plane with a dot ( $\phi_s'(z) = 0$ ), a line in the radial direction ( $\phi_s'(z) = 0$ ), and a circle ( $\phi_s'(z) \neq 0$ ), indicating the 1D, 2D, and 3D caustics, respectively; red arrows depict the transversal momentum along these trajectories by Eq. 3.

### 1.3 Intrinsic OAM: When Geometry Meets Symmetry.

Physical phenomena, demonstrating the objective features of nature, are unaffected by the observer's frame, such as the translational symmetry/invariance in the intrinsic angular momentum<sup>30</sup>. Unlike optical SAM, which remains independent of axis choice and hence inherently intrinsic with translational invariance, optical OAM is sensitive to the axis selection in



the general case<sup>29,31</sup>, comprising both intrinsic and extrinsic components (see details in ‘‘OAM theory of optical fields’’ of Supplementary Text 1). The extrinsic component is sensitive to the axis choice and disrupts translational invariance of optical OAM. When the transverse net momenta  $\mathbf{P}_\perp$  is zero<sup>29</sup>, the extrinsic constituent disappears, rendering the OAM purely intrinsic with translational invariance, e.g., intrinsic vortex-based OAM in conventional vortex beams like high-order Bessel beams and Laguerre–Gauss beams. Similarly, as long as the transverse net momenta  $\mathbf{P}_\perp$  in Eq. 6, which could be visualized by the phasor of  $I(z)\mathbf{p}_\perp(z)$  along the 3D caustic/mainlobe, is a zero vector, the vortex-free OAM is purely intrinsic with translational invariance. When  $I(z) = 1$  and  $z \in (a, b)$ , this condition of  $\mathbf{P}_\perp = 0$  in Eq. 6 is reduced to

$$(x_s(a), y_s(a)) = (x_s(b), y_s(b)) \leftrightarrow \mathbf{s}(a) = \mathbf{s}(b). \quad (7)$$

Equations 5-7 demonstrate that the vortex-free OAM within a uniform-strength ( $I(z) = 1$ ) self-accelerating beams exhibits intrinsic translational invariance, provided the 3D caustic—the self-accelerating mainlobe—ultimately resumes its original transversal position within the effective propagation range (i.e., trajectories are enclosed in the transversal position within  $\mathbf{s}(a) = \mathbf{s}(b)$  for  $z \in (a, b)$ ). This intrinsic nature is attributed to the absence of transverse net momentum<sup>29</sup>. The trajectory of the 3D caustic itself— $\mathbf{s}(z)$  within the defined range  $z \in (a, b)$ , dictates the magnitude of intrinsic vortex-free OAM, as described by Eq. 5.

For illustrative purposes, consider spirally self-accelerating Bessel-like beams depicted in Fig. 2E. These beams orbit through integer cycles over the effective propagation range within  $z \in (a, b)$ , and the 3D spiral caustic eventually returns to its original transversal position (i.e.,  $\mathbf{s}(a) = \mathbf{s}(b)$ ). Under these conditions, the transverse net momenta reduce to zero, rendering the global vortex-free OAM intrinsically invariant under translational symmetry. Conversely, if the 3D spiral caustic navigates fractional cycles without reverting to its original position (i.e.,  $\mathbf{s}(a) \neq \mathbf{s}(b)$ ), the transverse net momenta remain nonzero, and the vortex-free OAM acquires an extrinsic component that is sensitive to the axis choice and disrupts translational invariance. These dynamics will be experimentally validated in Fig. 3. This behavior parallels that observed in vortex beams with integer and fractional topological charges: the intrinsic translational invariance of the vortex-based OAM in beams with integer topological charges is maintained due to zero transverse net momentum<sup>29</sup>, whereas the presence of non-zero transverse net momentum in vortex beams with fractional topological charges introduces an extrinsic component, disrupting this invariance<sup>32</sup>. Furthermore, the localized vortex-free OAM along the 3D caustics is extrinsic, as articulated in Eq. 4 with  $\hbar k r_s^2(z) \varphi_s'(z)$ , similar to the extrinsic mechanical angular momentum of an orbiting free particle, as depicted in Eq. 2 with  $\hbar k r_s^2(t) \varphi_s'(t)$ . However, the global vortex-free OAM, governed by Eq. 5, remains intrinsic with the absence of transverse net momenta. This scenario is analogous to the behavior of vortex-based OAM: while the global OAM in vortex beams is intrinsic owing to zero transverse net momenta across the transverse plane, the localized OAM of any non-circularly symmetric area (similar to the OAM density) is extrinsic<sup>29</sup> due to non-zero transverse net momenta in that region. This correspondence underscores the necessity for structural integrity when detecting intrinsic OAM under translational invariance. Our analysis in this section establishes intrinsic vortex-free OAM as an inherent property of vortex-free structured fields arising from three-dimensional caustic trajectories.

## 2. Comprehensive Verification of Vortex-Free OAM Dynamics

### 2.1 Quantitative Validation of Vortex-Free OAM.

Our analysis of vortex-free OAM in self-accelerating beams begins with the angular spectrum, characterized by a tailored intensity profile  $I(z)$  and arbitrary 3D caustic trajectory of  $\mathbf{s}(z) = [x_s(z), y_s(z)]$  over the effective propagation distance  $z \in (a, b)$ , expressed as<sup>24</sup>

$$A(k_x, k_y) = \int_a^b \sqrt{I(z)} e^{ik_x x_s(z) + ik_y y_s(z)} e^{i\sqrt{k^2 - q^2}z} dz, \quad (8)$$

where  $(k_x, k_y, k_z)$  denote the wavenumbers in Cartesian coordinates, satisfying  $k^2 = k_x^2 + k_y^2 + k_z^2$ , and  $q$  represents the transverse wavevector component of the plane waves that constitute the Bessel-like beam. An illustrative example of parabolically self-

accelerating beams, similar to parabolic Airy beams, is depicted in Fig. S1. To establish vortex-free OAM as a fundamental property as outlined in Eq. 5, we employed multiple methodologies:

1. Momentum-Space Analysis<sup>31</sup>: We calculated vortex-free OAM using the angular spectrum of the self-accelerating beams, expressed as

$$J_z = \left( \int A^*(\mathbf{k}_\perp) \cdot (-i\mathbf{k}_\perp \times \frac{\partial}{\partial \mathbf{k}_\perp}) A(\mathbf{k}_\perp) d^2 \mathbf{k}_\perp \right) / \left( i \int A^*(\mathbf{k}_\perp) A(\mathbf{k}_\perp) d^2 \mathbf{k}_\perp \right), \quad \mathbf{k}_\perp = (k_x, k_y); \quad (9)$$

2. Real-Space Quantification<sup>31</sup>: We computed vortex-free OAM using the complex spatial distribution  $\psi(x, y, z)$  of the beams, expressed as

$$J_z = \left( \iint \psi^*(x, y, z) (\mathbf{r} \times \nabla) \psi(x, y, z) dx dy \right) / \left( i \iint \psi^*(x, y, z) \psi(x, y, z) dx dy \right); \quad (10)$$

3. Quantitative Experimental Measurement: the quantity of vortex-free OAM was determined utilizing the experimental technique outlined in Ref.<sup>33</sup>, which involves capturing two intensity distributions in the Fourier plane of orthogonally positioned cylindrical lenses and analyzing the first-order moments of these intensity distributions.

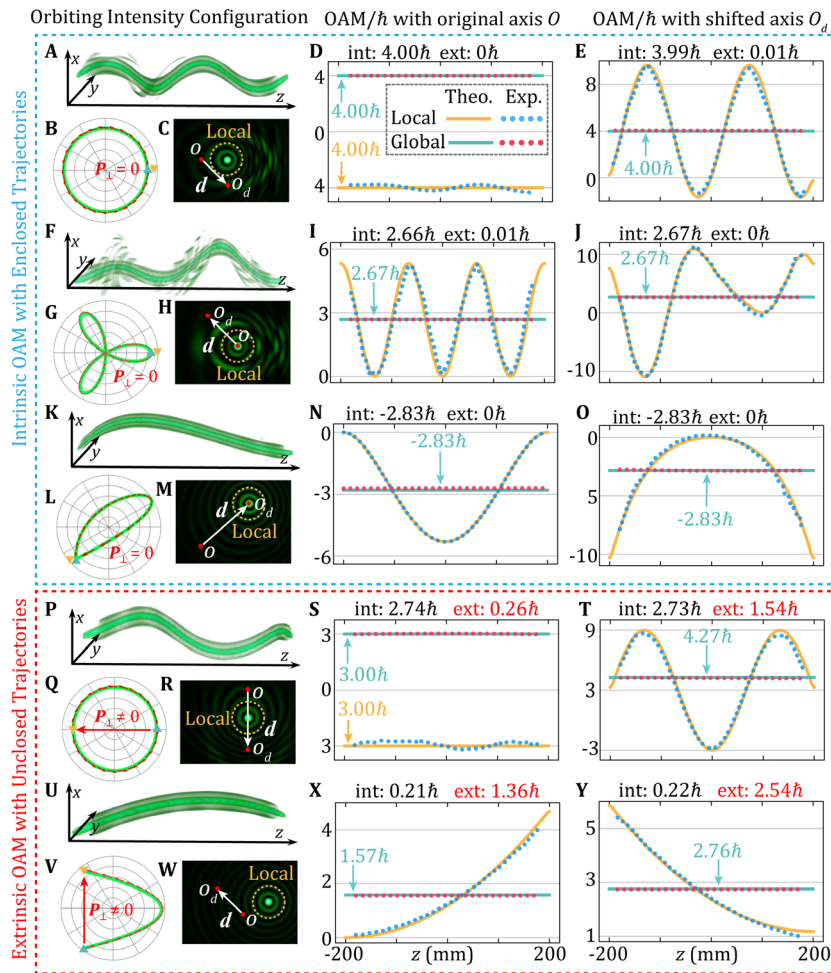


**Fig. 3.** Experimental validation of vortex-free OAM. Subgraphs (A-E) feature self-accelerating Bessel-like beam with enclosed spiral trajectory  $s(z)=0.1038[\cos(2\pi z/200), \sin(2\pi z/200)]$  mm, propagating within the range  $z \in (-200, 200)$  mm with the uniform-intensity  $I(z) = 1$ : (A) 3D intensity iso-surface; (B) 3D trajectory projection onto the  $x$ - $y$  plane, with cyan-up and orange-down triangles marking the start and finish points of the trajectory, respectively. Red arrows depicts the transversal momentum density  $p_\perp(z)$  and the phasor is zero ( $P_\perp = 0$ ) due to the enclosed trajectory. (C) Intensity map at  $z = 0$  mm, where the brown-dotted circle highlights the local region used for experimental OAM measurements along the mainlobe and the white arrow indicates the translation from the original axis  $O$  to the shifted axis  $O_d$ , with a shifted vector  $\mathbf{d} = (0.1038, -0.1038)$  mm; (D, E) Comparison between experimentally measured vortex-free OAM (the dotted curves) and theoretical predictions (the solid curves) from Eqs. 4 and 5 with the original axis  $O$  (D) and the shifted axis  $O_d$  (E). The values at the top indicate the calculated intrinsic (int) and extrinsic (ext) constituents. “Local” refers to local OAM along the 3D caustic, while “Global” represents global OAM across the transverse plane. “Theo.” and “Exp.” denote theoretical predictions and experimental

measurements, respectively. To avoid aliasing, both ends of the vertical axis in **(D)**, as well as **(S)**, are shown as positive. Other subgraphs follow the same structure as **(A-E)** but correspond to different trajectories  $s(z)$  and translation vectors  $\mathbf{d}$  (should not be parallel to  $\mathbf{P}_\perp$ ). Intrinsic vortex-free OAM cases: **(F-J)** Enclosed trefoil trajectory with  $s(z)=0.012[\cos(\pi z/200+\pi)+\cos(2\pi z/200), -\sin(\pi z/200+\pi)+\sin(2\pi z/200)]$  mm and  $\mathbf{d} = (-0.12, 0.12)$  mm; **(K-O)** Enclosed 3D parabolic trajectory with  $s(z)=0.3[(1-z/200)(1+z/200)^2, 1-z^2/200^2]$  mm and  $\mathbf{d} = (0.3, 0.3)$  mm. Counterexamples of extrinsic vortex-free OAM: **(P-T)** Unclosed spiral trajectory with 1.5 cycles in the propagation range with  $s(z)=0.1038[\cos(1.5\pi z/200), \sin(1.5\pi z/200)]$  mm and  $\mathbf{d} = (0, -0.2076)$  mm; **(U-Y)** Unclosed parabolic-linear trajectory with  $s(z)=0.2[1-z^2/200^2, 0.5(1+z/200)]$  mm and  $\mathbf{d} = (-0.2, 0.2)$  mm. Experiment visualizations of these OAM-carrying self-accelerating Bessel-like beams are available in Movie S2.

Matlab codes for the first and second methods and experimental details for the third are provided in Methods. For localized OAM validation along the 3D caustics (Eq. 4), an aperture was strategically used to pre-truncate the self-accelerating mainlobe in both the second and third methods. The results from three distinct methods consistently align with our theoretical predictions in Eqs. 4-5, ensuring a robust verification of our theoretical models. To ensure clarity in our plot presentation, our work primarily focus on comparing experimental results directly with theoretical predictions, as illustrated in Fig. 3.

Initially, intrinsic vortex-free OAM was measured in self-accelerating beams exhibiting transverse enclosed spiral, trefoil, and 3D parabolic trajectories within their propagation range, subsequently returning to their original transversal positions. These configurations are illustrated in Figs. 3A, 3F, and 3K. The experimental data, capturing both local and global values, closely align with our theoretical predictions in Figs. 3D, 3I, and 3N, with the calculated intrinsic and extrinsic components clearly delineated and marked in black, demonstrating negligible extrinsic components for these enclosed trajectories. Non-uniform intensity profiles (i.e.,  $I(z) \neq 1$ ) further confirm the framework's generality (Supplementary Text 2 with Movie S3). This multimodal convergence—spanning theory, computation, and experiment—provides important evidence that OAM could emerges fundamentally from photon path geometry, as well as phase topology.

## 2.2 Intrinsic Translational Invariance.

Translational invariance—the hallmark of intrinsic angular momentum. To validate the translational invariance of intrinsic vortex-free OAM, we shifted the optical axis from its original position,  $\mathbf{O} = (0, 0)$ , to a new position,  $\mathbf{O}_d = (x_d, y_d)$ , represented by the translation vector as  $\mathbf{d} = (x_d, y_d)$ , as depicted in Figs. 3C, 3H, and 3M. In the experiments, the actual optical axis remained fixed while the beam was translated by  $-\mathbf{d} = (-x_d, -y_d)$ . Following the Fourier phase-shifting theorem, the angular spectrum of the translated beam is expressed as  $A_d(k_x, k_y) = A(k_x, k_y) \exp(-ik_x x_d - k_y y_d)$ . Figures 3E, 3J, and 3O demonstrate that after translation, the global vortex-free OAM retains intrinsic translational invariance, while the local OAM along the mainlobes varies and exhibits extrinsic characteristics, mirroring the mechanical angular momentum of an orbiting free particle. Both intrinsic and extrinsic components, indicated by black numerical values at the top of each figure, show negligible extrinsic contributions, confirming the translational invariance of the global vortex-free OAM. Theoretical calculations of the transverse net momenta, represented by the phasor of the transversal momentum density  $I(z)\mathbf{p}_\perp(z)$  along the caustic/mainlobe, yield a zero vector for transversally enclosed trajectories, as depicted in Figs. 3(B), 3(G), and 3(L). The numerical calculation of these momenta is given by <sup>21</sup>

$$\mathbf{P}_\perp = \iint \frac{\epsilon_0}{2\omega} \text{Im}[\psi^*(x, y, z_0) \cdot (\nabla)\psi(x, y, z_0)] dx dy, \quad (11)$$

where  $z_0$  depicts arbitrary longitudinal plane (set to zero in this instance), shows that transverse net momentum vanishes for closed trajectories (Figs. 3A, 4F, and 4K), with residuals  $10^{-5}\hbar k$  per photon—consistent with experimental noise from finite aperture dimensions and sampling error in Matlab. Vortex-free OAM's intrinsic translational invariance potentially allows its application as a novel information carrier in communication systems<sup>34</sup>. By leveraging the complexity and unpredictability of vortex-free OAM, new approaches to optical security and encryption technologies could be developed, significantly enhancing data protection during transmission.

Conversely, instances where vortex-free OAM exhibits extrinsic characteristics are demonstrated through counterexamples with unclosed transversal trajectories, such as the 1.5-cycle spiral trajectory within the propagation range,



shown in Figs. 3P, and the non-closed parabolic-linear trajectory in Figs. 3U. These instances clearly show non-zero transverse net momenta, highlighted by a single red arrow marking the trajectory from start to finish (the Phasor), as evidenced in Figs. 3Q and 3V. Calculated transverse net momenta from these trajectories exceed  $10^{-3}\hbar k$  per photon for Figs. 3P and 3U, underscoring the variability in global OAM quantities with the translated axis, and the lack of translational symmetry/invariance, as validated in Figs. 3S-T and 3X-Y.

### 2.3 Mechanical Transfer: From Photonic Orbits to Macroscopic Rotation.

Optical tweezers<sup>35</sup>, originally proposed by Arthur Ashkin, the 2018 Nobel Laureate in Physics, serve as a powerful and noninvasive tool for manipulating microscopic particles. These instruments have become essential across various fields such as physics, biology, and soft condensed matter. The rotation of micro- and nano-objects within optical tweezers—facilitated by the transfer of angular momentum from light beams—is particularly noteworthy<sup>36</sup>. This process holds potential for revolutionary applications in the creation of optically driven micromachines, motors, actuators, and for the manipulation of biological specimens.

The ultimate test of intrinsic angular momentum lies in its mechanical transfer—a challenge vortex-free OAM passes decisively. Figure 4A depicts the experimental setup for optical manipulation, which incorporates an inverted confocal microscope (Nikon, TE2000-U) incorporated with a 4-f complex light field generator featuring a reflective spatial light modulator (SLM, Holoeye Leto). This setup utilizes a horizontally polarized collimated green laser beam (532 nm wavelength, Coherent, Verdi-v5), which is shaped and directed through an objective lens at a power of 90 mW. By modulated the angular spectrum  $A(k_x, k_y)$  from Eq. 8 to attain the computer-generated holograms loaded onto the SLM, this configuration generates the desired vortex-free self-accelerating fields in the focal area, which impact polystyrene microspheres (3.2  $\mu\text{m}$  in diameter) suspended in deionized water within a specially designed sample chamber. This chamber is constructed using an acrylic plate featuring a through-hole, with a glass cover slip at the base and an open top. The open-top design minimizes resistance from the sample chamber's upper boundary, allowing particles suspended in the solution within the hole to move freely at the water's surface without friction from a cover.

Consider the spirally self-accelerating beams illustrated in Fig. 4A—a vortex-free field with intrinsic vortex-free OAM of  $4\hbar$  per photon—as a case study. Particles are initially drawn towards the beam's mainlobes by the light's intensity-gradient force, following which they orbit along these mainlobes until reaching the liquid's surface, as shown in Fig. 4B. Upon reaching the liquid's surface (open-top), the particles rotate clockwise due to the conversion of optical OAM to mechanical angular momentum, as shown in Fig. 4C. When the vortex-free OAM is changed from  $4\hbar$  to  $-4\hbar$  by reversing the chirality of the spiral trajectory, the direction of particle rotation switches to counterclockwise, as demonstrated in Fig. 4D. Additional experiments with other types of vortex-free fields, such as the trefoil-shaped self-accelerating Bessel-like beams shown in Fig. 3F, also result in the rotation of trapped particles at the liquid surface through the mechanical transfer of intrinsic vortex-free OAM. Visualization of these experiments is available in Movie S4. Experiments show that optical fields lacking intrinsic vortex-free OAM (e.g., the Bessel-like beam with a parabolical trajectory in Fig. 2C), or those with minimal intrinsic components (e.g., the Bessel-like beam with the parabolic-linear trajectory in Fig. 3U), are unable to induce particle rotation at the liquid surface. Notably, particles exhibit solid core rotation (Fig. 4C-D), unlike vortex beams' hollow-core circulation of particles around the phase singularity, enabling compact micromotors. This optomechanical synergy confirms the existence of intrinsic vortex-free OAM, bridging optical and mechanical realms of vortex-free OAM and paving the way for optically-driven micromachines and biomimetic actuators<sup>36</sup>.

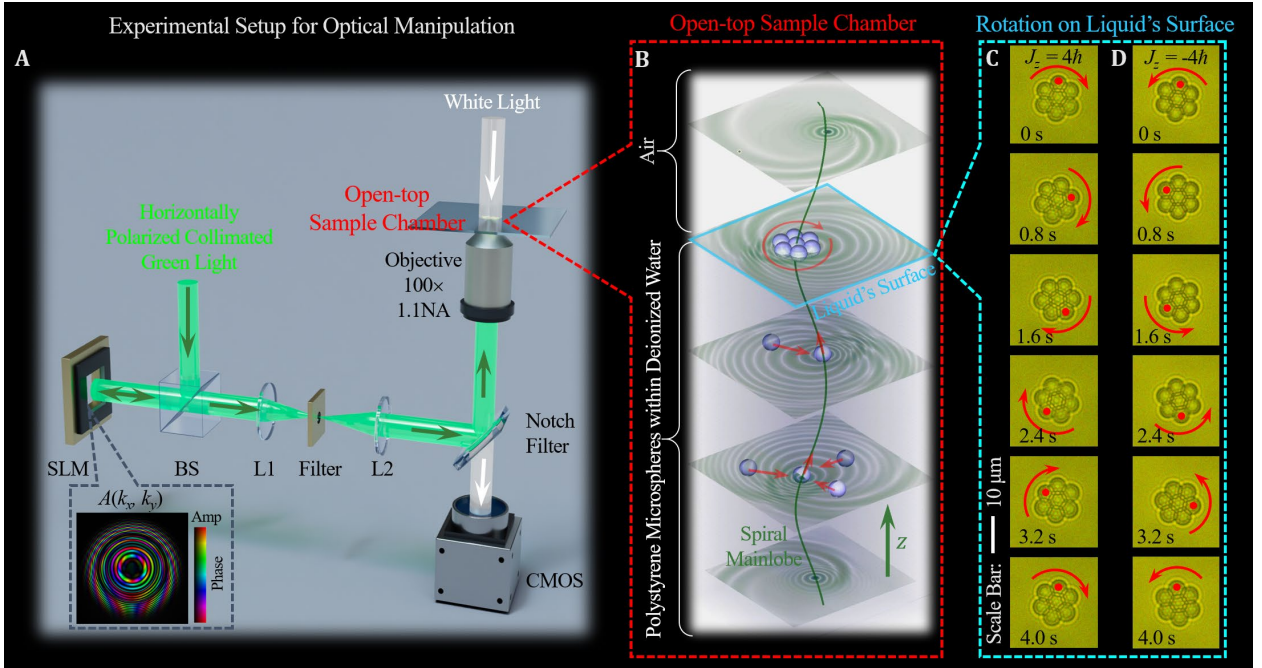


**Fig. 4.** Mechanical transfer of vortex-free intrinsic OAM in optical tweezers. (A) Schematic experimental setup for optical manipulation. BS, beam splitters; SLM, phase-only spatial light modulator; L1–2, lenses. The inset depicts the angular spectrum  $A(k_x, k_y)$  of a spirally self-accelerating beam from Eq. 8, loaded on SLM after modulation. Subgraph (B) depicts the open-top sample chamber with the spirally self-accelerating beam, carrying intrinsic vortex-free OAM of  $4h$  per photon, incident from below: the polystyrene microspheres are initially drawn towards the beam's mainlobe and orbit along this mainlobe until reaching the liquid's surface; the particles finally rotate clockwise on the open-top liquid's surface, with the frame images in (C). When changing the intrinsic vortex-free OAM from  $4h$  to  $-4h$  by reversing the chirality of the spiral trajectory, the direction of particle rotation switches to counterclockwise in (D). Experiment visualizations are available in Movie S4.

Our experimental and theoretical analyses have established a fundamental mechanical correspondence: just as celestial orbits inherently carry angular momentum through path geometry, structured light generates intrinsic OAM through 3D caustic trajectories—no phase vortices required. This mechanical analogy, validated through numerical simulations (Matlab codes in Methods), precision interferometry (Fig. 3), and optomechanical transfer in tweezers (Fig. 4), reveals a tripartite hierarchy of optical angular momentum:

- Spin angular momentum - Photon spin about self-axis (circular polarization)
- Vortex-based OAM - Collective photon rotation about beam axis (helical wavefronts)
- Vortex-free OAM - Photon orbital motion along curved caustics (geometric path curvature)

This taxonomy resolves the historical dichotomy between spin and orbital angular momentum by introducing geometric curvature as a third fundamental mechanism—a conceptual leap echoing Poynting's original mechanical vision<sup>1</sup> and Allen's vortex revolution<sup>4</sup>, but now generalized to encompass all structured light including vast vortex-free fields. Crucially, it was demonstrated that intrinsic OAM can manifest not only through phase singularities but also through photon trajectories: closed caustic paths (Figs. 3A–O) generate intrinsic components, while open paths produce measurable extrinsic components (Figs. 3P–Y). This geometric framework, however, reveals deeper questions: How do these distinct angular momentum mechanisms coexist in complex optical fields? Can we unify their description under universal principles? To address this, our research now transcends mechanical analogies through a hydrodynamic reframing of light's rotational dynamics.

### 3. Universal Optical OAM Analysis through Hydrodynamic Insights

#### 3.1 Unifying OAM Analysis through Energy Streamlines.

Angular momentum serves as a universal descriptor of rotational dynamics across physical systems, yet conventional optical models have historically fragmented its analysis. Vortex beams, exemplified by high-order Bessel and Laguerre-Gaussian modes, exhibit rotational energy dynamics through their spiral phase fronts. Conversely, vortex-free fields—such as spiral and trefoil self-accelerating beams—demonstrate orbital energy dynamics via 3D caustic trajectories. Traditional wavefront-centric models, while effective for vortex characterization, inadequately capture the full spectrum of energy dynamics in structured fields. To bridge this gap, a hydrodynamic analogy that reimagines light propagation through the lens of fluid motion is adopted.

The analogy between the dynamics of lasers and fluid/superfluids systems has been evident since the early 1970s, when laser physics equations were reduced into the complex Ginzburg–Landau equations<sup>37</sup>. This framework has since been widely applied to elucidate phenomena such as superconductivity, superfluidity, and Bose-Einstein condensation<sup>38</sup>. This analogy has fostered a deeper exploration of hydrodynamic behaviors within optical fields<sup>39–41</sup>, examining aspects like chaos, multistability, and turbulence, which have been observed both theoretically and experimentally in laser systems<sup>42–44</sup>. For instance, Coulet et al., inspired by hydrodynamic vortices, formally proposed the concept of optical vortices<sup>3</sup> in 1989. Building on this foundational understanding, we adopt a hydrodynamic approach to transform OAM analysis based on the energy streamlines<sup>45,46</sup>—integral curves of the Poynting vector. In greater detail, the Poynting vector  $\mathbf{p}(\mathbf{R})$  for a scalar wave  $\psi(\mathbf{R})$  with  $\mathbf{R} = \{x, y, z\}$ , the expectation value of the local momentum operator<sup>45</sup>, can be expressed as

$$\mathbf{p}(\mathbf{R}) = \text{Im} \psi^*(\mathbf{R}) \nabla \psi(\mathbf{R}) = |\psi(\mathbf{R})|^2 \nabla \arg \psi(\mathbf{R}), \quad (12)$$

This expression is an important ingredient in calculating the OAM of the field<sup>47</sup>. The trajectories  $\mathbf{R}(z) = \{x(z), y(z), z\} = \{r(z), \varphi(z), z\}$  of energy streamlines can be obtained in either Cartesian or cylindrical coordinate systems by solving the hydrodynamic differential equations:

$$dx(z)/dz = p_x(\mathbf{R}(z))/p_z(\mathbf{R}(z)), \quad dy(z)/dz = p_y(\mathbf{R}(z))/p_z(\mathbf{R}(z)); \quad (13-1)$$

$$dr(z)/dz = p_r(\mathbf{R}(z))/p_z(\mathbf{R}(z)), \quad d\varphi(z)/dz = p_\varphi(\mathbf{R}(z))/[r(z)p_z(\mathbf{R}(z))]; \quad (13-2)$$

where  $\mathbf{p} = \{p_x, p_y, p_z\} = \{p_r, p_\varphi, p_z\}$ . These energy streamlines, often likened to "Bohmian trajectories" of light propagation, represent experimentally measurable paths of average photon trajectories<sup>45,48–50</sup>. In quantum physics, the trajectories of the Poynting vector in light (or quantum-mechanical waves) are described as streamlines in the Madelung hydrodynamic interpretation<sup>51</sup>, which are later regarded as paths of quantum particles in the Bohm–de Broglie interpretation<sup>52,53</sup>.

By mapping energy streamlines—photon analogues of fluid trajectories—our results uncover universal OAM generation mechanisms:

- Vortex Beams (Figs. 5A-B) with intrinsic OAM: Helical streamlines with 3D curvature ( $\varphi'(z) \neq 0$  in Eqs. 14-15) generate intrinsic OAM via coordinated photon rotation, akin to water spiraling down a drain.
- Vortex-Free Beams (Figs. 5D-E) with intrinsic OAM: Orbital streamlines with 3D curvature ( $\varphi'(z) \neq 0$  in Eq. 16-17) transfer intrinsic OAM through path curvature, mimicking planets' orbital angular momentum.
- Vortex-Free Beams (Figs. 5F-G) without OAM: Streamlines without 3D curvature ( $\varphi'(z) = 0$ ).

This hydrodynamic model unifies traditional vortex-based OAM and vortex-free OAM under a single framework, revealing that both originate from rotational or orbital streamline with 3D curvature ( $\varphi'(z) \neq 0$ ). For the Bessel beam and Laguerre-Gaussian beam with  $l = 0$  (Figs. 5F-G), where there is neither a spiral phase nor an orbital intensity configuration, the energy streamlines exhibit no rotational or orbital dynamics without 3D curvature ( $\varphi'(z) = 0$ ), thus excluding the presence of OAM.

Ideally, a complete description of the optical field would require an infinite continuum of energy streamlines, with their local density accurately mapping the spatial variation of light intensity. However, practical limitations—namely, the finite sampling capacity of current computational resources and the need for clear, interpretable visualizations—compel us to adopt a simplified representation. Consequently, in Fig. 5, we selectively plot a finite number of characteristic streamlines. To compensate for this discretization and to convey the underlying multiplicity of photon trajectories within a given region, the brightness of each streamline are modulated in accordance with the local intensity. This approach preserves the essential physical insights of the continuous energy-flow dynamics while ensuring both computational efficiency and visual clarity.

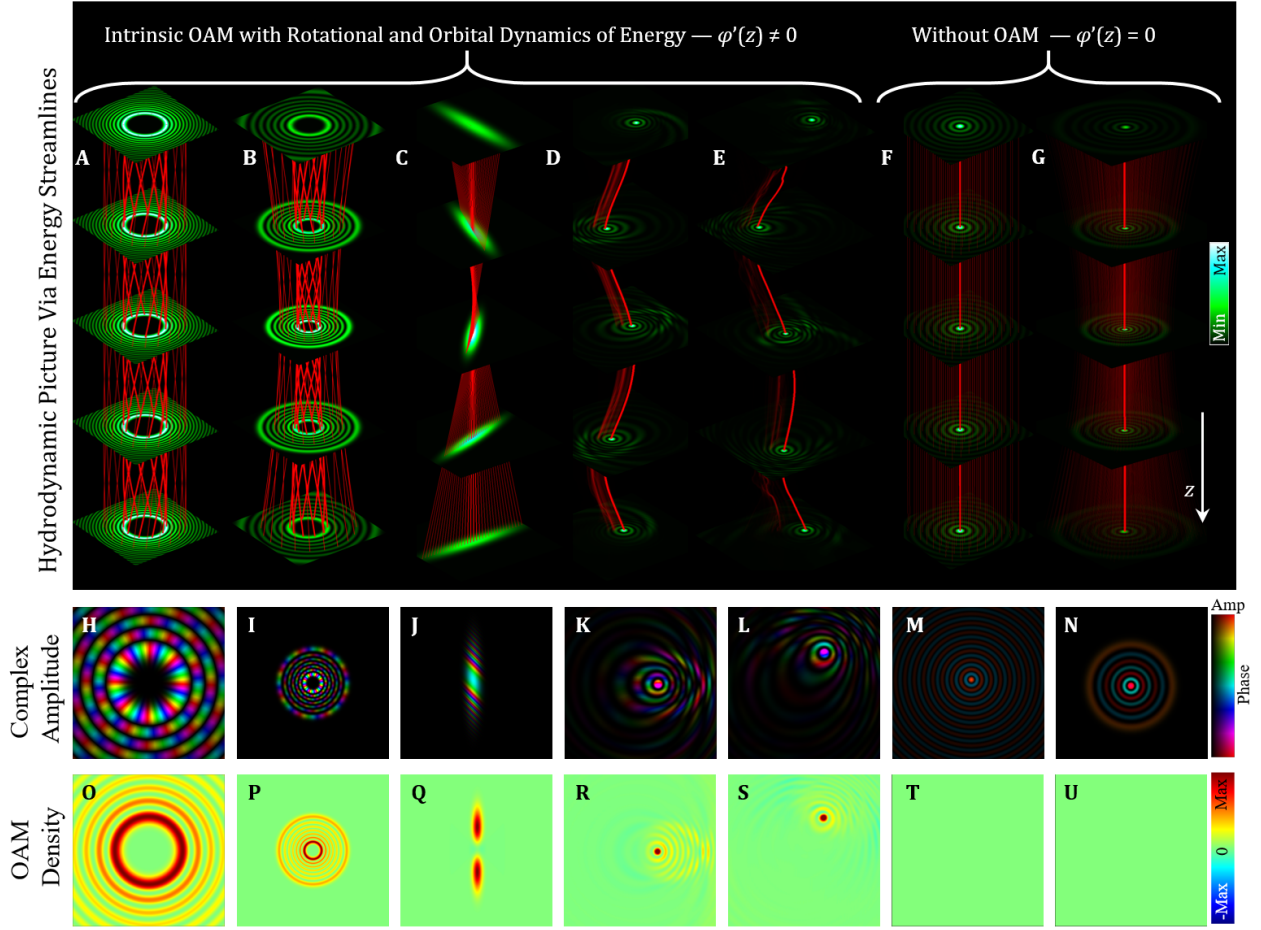


**Fig. 5.** Hydrodynamic picture via energy streamlines. The helical energy streamlines, depicted by the red curves, in (A) high-order Bessel beams and (B) Laguerre-Gaussian beams indicate the rotational dynamics of energy. The rotational energy streamlines of (C) an elliptical Gaussian beam focussed by a tilted cylindrical lens<sup>20</sup> indicate the orbital dynamics of energy. The orbiting energy streamlines along the mainlobes of spirally (D) and trefoilly (E) self-accelerating Bessel-like beams in Figs. 3(A) and (F), indicate the orbital dynamics of energy in vortex-free structured beams. For the (F) Bessel beam and (G) Laguerre-Gaussian beam with  $l = 0$ , without any spiral phase and 3D orbital intensity configuration, the streamlines exhibits neither rotational nor orbital dynamics of energy with  $\varphi'(z) = 0$ , and consequently precludes OAM. The streamlines herein are directly drew from the “streamline” function with the distributions of Poynting vector calculated in Matlab, which are consistent with the analytical solutions from the hydrodynamic differential equations in this work. (H-N) The corresponding complex amplitude distributions and (O-U) OAM density distributions at  $z = 0$ . The corresponding OAM density distributions up propagation are provided in Movie S5.

From caustic trajectories (photon 'orbital highways') to energy streamlines (the complete 'roadmap' of photon motion), this hydrodynamic insight can also offer a universal framework for quantifying angular momentum through measurable streamline curvature. This hydrodynamic framework involves several key steps:

1. Within this hydrodynamic perspective, each energy streamline of light can be conceptualized as a 3D orbiting configuration of localized energy, following the trajectory  $\mathbf{R}(z) = \{x(z), y(z), z\} = \{r(z), \varphi(z), z\}$ .
2. The OAM associated with 3D orbiting configurations along the trajectories  $\mathbf{R}(z)$  can be quantified employing the mechanical analogy, as outlined in Eq. 4.
3. The global OAM of given optical fields is determined by performing an energy-weighted averaging of OAM contributions across all energy streamlines.

This framework provides a comprehensive quantification of optical OAM across diverse beam configurations in the hydrodynamic perspective. Detailed elaborations on this hydrodynamic methodology are provided below:



**Case Study 1—Vortex beams.** In the realm of vortex beams, the trajectories of energy streamlines<sup>45</sup> within high-order Bessel beams are expressed as

$$\mathbf{R}(z) = \{r(z), \varphi(z), z\} = \left\{ r_0, \varphi_0 + \frac{l}{r_0^2 \sqrt{k^2 - q^2}} z, z \right\}, \quad (14)$$

where  $r_0$  and  $\varphi_0$  is the initial position of the streamlines. These energy streamlines are helical paths winding on cylinders, as illustrated in Fig. 5A. For Laguerre-Gaussian beams, the trajectories of energy streamlines<sup>45</sup> are expressed as

$$\mathbf{R}(\zeta) = \{\rho(\zeta), \varphi(\zeta), \zeta\} = \left\{ \rho_0 \sqrt{1 + \zeta^2}, \varphi_0 + \frac{l}{\rho_0^2} \arctan \zeta, \zeta \right\}, \quad (15)$$

in scaled coordinates  $(r, \varphi, z) \equiv (\omega_0 \rho, \varphi, k \omega_0^2 \zeta)$ , where  $\omega_0$  is the waist radius,  $\rho_0$  and  $\varphi_0$  is the initial position of the streamlines in these coordinates. These energy streamlines of Laguerre-Gaussian beams also exhibit helical trajectories, but in this case, they wind around hyperboloidal surfaces, as depicted in Fig. 5B. These helical configurations of energy streamlines in hydrodynamic picture—characteristic of vortex beams—reveal the underlying rotational dynamics of energy under the circular symmetric intensity profiles of these beams. By substituting the trajectories  $\mathbf{R}(z)$  of Eqs. 14-15 into Eq. 4 with  $\hbar k r^2(z) \varphi'(z)$ , the result demonstrates that the OAM of each helical energy streamline, arising from 3D orbiting configurations of localized energy, consistently equals  $l\hbar$  per photon. Consequently, the global OAM of Bessel and Laguerre-Gaussian beams in this hydrodynamic framework—the energy-weighted average of OAM across all streamlines—are also  $l\hbar$  per photon, aligning with electrodynamic outcome in Eq. 10.

**Case Study 2—Vortex-free fields.** Courtial, Dholakia, Allen, and Padgett introduced a concise model<sup>20</sup> in 1997, demonstrating that an elliptical Gaussian beam, focused by a tilted cylindrical lens, exhibits vortex-free OAM. This model, described by the expression  $\sqrt{\exp(-2x^2/w_x^2 - 2y^2/w_y^2)} \exp(ik(x \sin \alpha + y \cos \alpha)^2 / 2f)$ , where  $w_x$ , and  $w_y$  denote the beam widths, and  $\alpha$  and  $f$  are the aligned angle and focal length of the cylindrical lens, respectively, marked the inception of vortex-free OAM studies. Notably, the absence of transverse net momentum in this beam configuration confirms its intrinsic vortex-free OAM. The trajectories of energy streamlines with  $\alpha = \pi/4$  are expressed as

$$\mathbf{R}(z) = (x(z), y(z), z) = \left( x_0 + \frac{z}{2f} (y_0 - x_0), y_0 + \frac{z}{2f} (x_0 - y_0), z \right) \quad (16)$$

where  $x_0$  and  $y_0$  are the beginning position of the streamlines. These energy streamlines—tilted lines with 3D curvature ( $\varphi'(z) \neq 0$ ) when  $y_0 \neq x_0$ , as observed in Fig. 5C, reinforce the rotational dynamics. The OAM of each energy streamline is  $\hbar k (x_0^2 - y_0^2) / 2f$ , determined using Eq. 4. The global OAM—the energy-weighted average of OAM across all energy streamlines with the energy weight  $\exp(-2x_0^2/w_x^2 - 2y_0^2/w_y^2)$ , aligns with theoretical predictions<sup>20</sup> and electrodynamic outcomes<sup>31</sup> by Eq. 10. For instance, when  $(w_x, w_y, f) = (1 \text{ mm}, 0.1 \text{ mm}, 100 \text{ mm})$  and  $(1 \text{ mm}, 0.2 \text{ mm}, 200 \text{ mm})$ , the global OAM calculated by analyzing energy streamlines is  $14.61\hbar$  and  $7.08\hbar$ , respectively, which are consistent with electrodynamic outcomes by Eq. 10 as  $14.51\hbar$  and  $7.07\hbar$ , with negligible error.

**Case Study 3—Vortex-free Self-accelerating Beams.** In the context of vortex-free self-accelerating beams with intrinsic OAM, such as the spiral and trefoil self-accelerating beams depicted in Figs. 3A and 3F, it is not feasible to derive explicit complex expressions for calculating the analytical solutions of all energy streamlines. Nevertheless, the geometrical mapping between transverse and longitudinal dimensions along the caustic mainlobes, as illustrated in Fig. 2, demonstrates that the integration of energy, momentum, and OAM within any transverse plane is equivalent to their integration along the caustic mainlobe. Consequently, our analysis concentrates on the energy streamlines within the volume of the self-accelerating mainlobe. The transversal Poynting vector along these mainlobes, as delineated in Eq. 3 as  $\hbar k s'(z)$ , is directly proportional to the derivative of the self-accelerating trajectories  $s(z) = (x_s(z), y_s(z))$ . According to hydrodynamic differential equations, the energy streamlines that originate at the mainlobe  $(x_s(z_0), y_s(z_0), z_0)$  align with the self-accelerating trajectories, given by

$$\mathbf{R}(z) = \{x(z) = x_s(z), y(z) = y_s(z), z\}. \quad (17)$$



These orbiting streamlines along the self-accelerating mainlobes, as observed in Figs. 5D and 5E, elucidate the orbital dynamics of energy within these regions along the 3D caustics. Therefore, the intrinsic vortex-free OAM in these self-accelerating beams, as calculated by Eqs. 4-5, is consistent with predictions from the hydrodynamic framework.

**Case Study 4—Optical fields without OAM.** In contrast, optical fields without OAM, such as the Bessel and Laguerre-Gaussian beams with  $l = 0$ , do not exhibit rotational or orbital energy dynamics, as demonstrated in Figs. 5F and 5G. The energy streamlines in these cases, characterized by  $R(z) = \{r_0, \varphi_0, z\}$  and  $\{\rho_0 \sqrt{1 + \zeta^2}, \varphi_0, \zeta\}$ , fail to generate OAM, in accordance with the condition  $\varphi'(z) = 0$  in Eq. 4, which implies the absence of OAM.

In stark contrast to traditional wave and ray models that typically capture only the superficial aspects of optical fields, this hydrodynamic framework—conceptualizing optical fields as energy streamlines—unifies traditional vortex-based OAM and vortex-free OAM under a single paradigm, revealing that both originate from rotational or orbital energy flows and are measurable via streamline curvature.

### 3.2 Extending to Hybrid Optical Structures.

The hydrodynamic model’s power lies in its capacity to unify disparate OAM phenomena. Vortex-based and vortex-free OAM coexist in hybrid fields, creating intertwined rotational and orbital dynamics. Self-accelerating vortex beams exemplify this synergy: their annular vortex cores follow predefined caustic paths, generating hybrid OAM with distinct intrinsic components (Fig. 6). This behavior is reminiscent of natural vortex phenomena such as galactic spirals and tornadoes. The generation of self-accelerating vortex beams can be achieved by superimposing a vortex phase, expressed as  $\exp(il\phi)$ , onto the angular spectrum of a zeroth-order self-accelerating Bessel-like beam, whose trajectory is given by  $s(z) = [x_s(z), y_s(z)]$  from Eq. 8. The resulting beam acquires characteristics similar to those of higher-order Bessel beams, with an annular vortex mainlobe that follows the predefined self-accelerating path  $s(z)$ , as depicted in Figs. 6A-C. The geometrical-optics rays of these self-accelerating vortex beams consist of skew rays arrayed on translational hyperboloidal surfaces. Their 3D caustics form a tubular structure along the self-accelerating annular vortex mainlobe—illustrated by the red-dotted curves in Figs. 6D-F. These caustics arise from the transverse circular caustics (red circles) of the hyperboloidal surfaces.

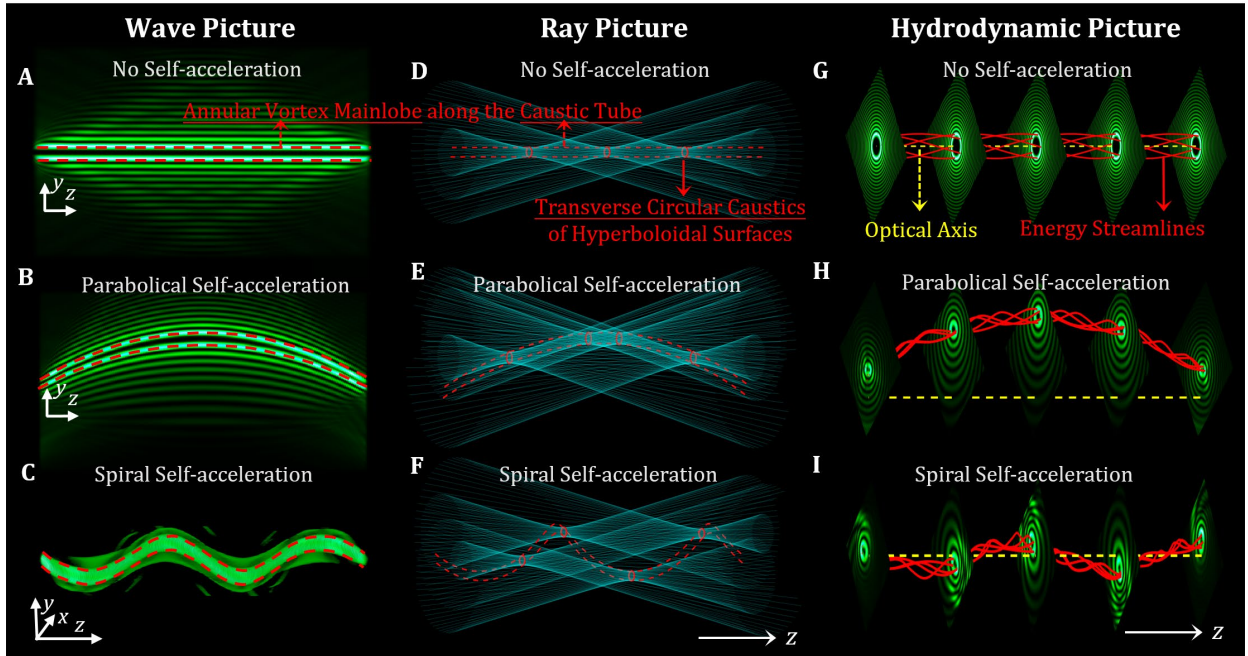


**Fig. 6.** Wave, ray and hydrodynamic pictures of self-accelerating vortex beams. Subgraphs (A-C) features vortex beams with no, parabohical, and spiral self-acceleration, and the red-dotted lines depicts the trajectories of annular vortex mainlobes.

Subgraphs (D-F) features that the geometrical-optics rays (the cyan lines) of self-accelerating vortex beams in (A-C) are lying on hyperboloidal surfaces and the caustic “tubes” (the red-dotted lines) are constituted by the transverse circular caustics (red circles) of hyperboloidal surfaces. Subgraphs (G-I) features that by conceptualizing optical fields as energy streamlines (red curves), this hydrodynamic framework clarifies the intertwined rotational and orbital dynamics within the caustic “tubes” (annular vortex mainlobes) of self-accelerating vortex beams. The yellow-dashed lines indicate the optical axis. The streamlines are directly drew from the “streamline” function with the distributions of Poynting vector calculated in Matlab, which are consistent with the analytical solutions from the hydrodynamic differential equations.

**Case Study 5—Hybrid structured fields.** By conceptualizing optical fields as energy streamlines, the hydrodynamic framework can clarify the intertwined rotational and orbital dynamics within these beams while quantifying the different OAM components within hybrid configurations. According to the hydrodynamic differential equations, the energy streamlines within the volume of the self-accelerating annular vortex mainlobe, outlined as

$$\mathbf{R}(z) = (x_s(z) + r_0 \cos(\varphi(z)), y_s(z) + r_0 \sin(\varphi(z)), z), \text{ where } \varphi(z) = \varphi_0 + \frac{l}{r_0^2 \sqrt{k^2 - q^2}} z, \quad (18)$$

encapsulate the combined dynamics of high-order Bessel beams (Eq. 14) and self-accelerating Bessel-like beams (Eq. 17). This integration elucidates the hybrid rotational and orbital motion, as observed in Figs. 6G-I. The hybrid OAM of these self-accelerating vortex beams, based on the analysis of energy streamlines and the geometrical mapping relationship of Bessel-like beams, is quantified as

$$J_z = \hbar k \left\langle I(z)(x_s(z)y_s'(z) - y_s(z)x_s'(z)) \right\rangle_z / \langle I(z) \rangle_z + l\hbar. \quad (19)$$

The first component of Eq. 19 corresponds to vortex-free OAM, similar to Eq. 5, arising from the orbital energy distribution within the self-accelerating beam. In contrast, the second component originates from the rotational energy dynamics of the optical vortex mainlobe, constituting the vortex-based OAM. Momentum analysis indicates that the vortex-based OAM is always intrinsically linked to the presence of optical vortices, whereas the vortex-free component acquires intrinsic properties when conditions satisfy Eq. 7, particularly in the absence of transverse net momentum. This comprehensive representation of hybrid OAM aligns with theoretical predictions from electrodynamics and spatial distribution results described in Eq. 10. Detailed derivations and experimental validations are provided in the Supplementary Text 3 with Movie S6. Experimental validation via optical tweezers (Movie S7) confirms the mechanical equivalence of both OAM forms:

The foundational work by Simpson, Dholakia, Allen and Padgett in 1997 established the mechanical equivalence between intrinsic SAM and intrinsic vortex-based OAM through additive/cancellative rotational effects in circularly polarized vortex beams<sup>54</sup>. Building upon this spiral self-accelerating vortex beams (Fig. 6C), our research experimentally validate the mechanical equivalence between intrinsic vortex-free OAM and intrinsic vortex-based OAM. Employing the optical manipulation setup depicted in Fig. 4A, these hybrid beams are engineered where:

- Vortex-free OAM component: Maintains time-invariant clockwise spiral trajectories (fixed at  $2\hbar$  per photon);
- Vortex-based OAM component: Features dynamically tunable topological charges ( $l = 4, 2, 0, -2, -4$ ).

This configuration generates total hybrid OAM values of  $(l+2)\hbar$  per photon. By dynamically tuning vortex topological charge while maintaining fixed vortex-free OAM, the experimental results exhibit predictable transitions in microparticle rotation states (Movie S7): high-speed clockwise rotation (total hybrid OAM of  $6\hbar$ ), mid-speed clockwise rotation (total hybrid OAM of  $4\hbar$ ), low-speed clockwise rotation (total hybrid OAM of  $2\hbar$ ), critical near-static state (total hybrid OAM of  $0\hbar$ ), and direction-switched counter rotation (total hybrid OAM of  $-2\hbar$ ). The observed monotonic relationship between hybrid OAM magnitude and rotational velocity conclusively demonstrates the mechanical equivalence between these two forms of intrinsic OAM. Future investigations will extend this equivalence framework to SAM and vortex-free OAM interactions through birefringent particle manipulation with circularly polarized vortex-free beams, potentially unifying the three intrinsic angular momentum categories (SAM, vortex-based OAM, vortex-free OAM) under a single mechanical paradigm.

A traditional synthesis of relevant research<sup>27,29-32,54</sup> on optical OAM highlights that "the extrinsic OAM is associated with the geometrical optics trajectory of the beam centroid, while the intrinsic OAM describes energy flows taken to the

center of the field (e.g., vortices)<sup>31</sup>. This universality in our work may resolve long-standing ambiguities in OAM categorization: Vortex-based OAM arises from rotational energy flows near phase singularities, while vortex-free OAM originates from orbital energy redistribution along caustics; Both forms achieve intrinsic translational invariance when transverse net momenta vanish, enabling their coexistence in engineered fields. Such hybrid systems emulate natural fluid phenomena—galactic spirals or tornadoes’ simultaneous rotation and orbital motion—while offering fine control over light’s angular momentum architecture.

### 3.3 Demonstrating the Universal Applicability.

Through detailed analyses presented in Case Study 1-5, this framework has demonstrated its effectiveness across a spectrum of optical configurations. To validate its universality to general optical fields, the congruence between hydrodynamic framework and electrodynamics in quantifying optical OAM is demonstrated: Given that the trajectory  $\mathbf{R}(z)$  represents the integral curves of the Poynting vector by hydrodynamic differential equations, the OAM calculated along these trajectories (using Eq. 4) can be interpreted as the OAM density distribution (per photon) along that specific path  $\mathbf{R}(z)$  in the light field. When performing an energy-weighted averaging of OAM across all trajectories emanating from an initial plane, it is essentially integrating the OAM density (per photon) across this plane to derive the global OAM for the entire fields in electrodynamics. The derivations are provided in the Supplementary Text 4. Consequently, the hydrodynamic approach provides a visually intuitive and physically robust framework to perceive and quantify OAM that aligns with the established definitions of optical OAM in electrodynamics<sup>21,31</sup>. This alignment ensures its universality and broad applicability to understand and manipulate the angular momentum in diverse optical settings.

Conclusively, our research expands our understanding of how both vortex and vortex-free OAM originate from rotational and orbital energy streamlines from hydrodynamic insight. This hydrodynamic framework not only quantifies angular momentum through measurable streamline curvature but also enables predictive design of hybrid light fields combining multiple OAM modalities (Fig. 6). By bridging optics and fluid dynamics, the evidence of hydrodynamic framework addresses the long-standing dichotomy between vortex and vortex-free OAM, offering a unified language to describe rotational dynamics across vortex and vortex-free regimes. This model, relying on energy streamline geometry—rather than ad hoc phase or intensity features, could establish OAM as a universal geometric property of structured light—-independent from phase singularities. The potential implications span optical manipulation, where "fluidic" light fields could enable biomimetic particle steering, to quantum communications, offering high-dimensional encoding via hybrid OAM states. Future work may extend this framework to spin-orbit interactions and non-paraxial regimes, suggesting potential applications in hydrodynamic photonics.

## Discussion and Conclusion

For three decades, the intrinsic OAM of light has been inextricably tied to phase vortices—a paradigm rooted in Allen’s landmark 1992 discovery. Here, our work uncovers a third category of optical angular momentum: vortex-free intrinsic OAM, arising not from helical wavefronts but from three-dimensional caustic trajectories in structured light fields. Through numerical modeling, precision experiments, and direct mechanical transfer of OAM to particles in optical tweezers, it was demonstrated that this previously overlooked form of angular momentum is a universal property of vortex-free fields, governed by a hydrodynamic analogy between light’s energy streamlines and orbital motion in fluid dynamics.

The experimental evidence addresses a persistent dichotomy in optical physics. While Berry’s theoretical work<sup>21-22</sup> hinted at the independence of OAM from vortices, the physical manifestation of intrinsic angular momentum in vortex-free fields remained experimentally unconfirmed. By extending Poynting’s mechanical framework beyond spin dynamics, our research establishes that curved caustic trajectories act as photon "orbital highways," generating quantifiable OAM through path geometry alone. This mirrors celestial mechanics, where planetary orbits inherently carry angular momentum independent of rotational spin—a symmetry now introduced to structured light. Crucially, our hydrodynamic model unifies

traditional vortex-based OAM and vortex-free OAM under a single paradigm, revealing that both originate from rotational or orbital energy flows measurable via streamline curvature.

The potential implications may span foundational science and applied technologies. By decoupling OAM from phase singularities, our work could inform future developments in diverse optical systems—from non-diffracting beams to dynamically tailored fields—unlocking potential applications in high-dimensional optical communications, quantum state manipulation, and biomimetic optofluidics. The mechanical transfer of vortex-free OAM to microparticles, demonstrated here, underscores its tangible physicality and paves the way for optically driven micromachines free of vortex constraints. By bridging optics and fluid mechanics<sup>7</sup>, this hydrodynamic framework transcends the vortex-centric worldview, and could offer a universal lens to explore angular momentum across structured fields—a conceptual framework with significant implications for both classical and quantum photonics.

## Methods

### Measurement of Vortex-free OAM

The Matlab codes for numerically computing OAM of vortex-free self-accelerating beams have integrated to the repository of Github at <https://github.com/WenxiangYan/OAM>.

According to the method proposed in ref.<sup>33</sup>, the OAM can be measured using the equation:

$$J_z \approx \frac{\hbar k}{f_c} \left( \iint_{-\infty}^{\infty} x \xi I_{y_f}(x, \xi) dx d\xi - \iint_{-\infty}^{\infty} \eta y I_{x_f}(\eta, y) d\eta dy \right) / \left( \iint_{-\infty}^{\infty} I_{x_f}(\eta, y) dx dy \right), \quad (20)$$

where  $f_c$  is the focal length of a pair of cylindrical lenses with perpendicular focusing dimensions (i.e., the  $x$ - and  $y$ -dimensions).  $I_{x_f}(\eta, y)$  and  $I_{y_f}(x, \xi)$  are the intensity distributions of the focal planes of the cylindrical lenses focusing along the  $x$  and  $y$  dimensions, respectively. The coordinates of these planes are  $(\eta, y)$  and  $(x, \xi)$ , which can be measured by CMOS2 and CMOS3 as shown in Fig. 7.

**Generation.** The experiment setup is shown in Fig. 7: A reflective SLM (Holoeye GAEA-2), imprinted with computer-generated hologram patterns (the Fourier marks), transforms a collimated laser light wave into a complex field corresponding to the angular spectrum of self-accelerating Bessel-like beams in real-space coordinates, with the help of spatial filtering via a 4-F system consisting of lenses L1 and L2, and a filter F1 as well. The resulting field is responsible for generating self-accelerating Bessel-like beams in the focal volume of lens L3.

**Detection.** A delay line, consisting of right-angle and hollow-roof prism mirrors and a translation stage, enables the different cross-sections of self-accelerating Bessel-like beams to be imaged on a complementary metal-oxide semiconductor camera CMOS1 (Dhyana 400BSI from LBTEK) after passing through a relay 4-F system consisting of two lenses. The combination of the delay line and the relay system enables the recording of intensity cross-sections at different  $z$ -axial locations relative to the focal plane of lens L3.

**Global OAM Measurement.** Beam splitter BS2 divides the beam, directing one part to CMOS1 for imaging and the other to a pair of cylindrical lenses for OAM measurement. The optical field at the focal plane of L5 is focused onto CMOS2 and CMOS3 (PCO. edge 4.2bi), enabling the calculation of global OAM using Eq. 20. The combination of the delay line, the relay system, and the OAM measurement section work together to measure global OAM at different  $z$ -axial locations.

**Local OAM Measurement.** A filter, fabricated with photoetched chrome hole patterns on a glass substrate, is inserted at the front focal plane of L4 to intercept the self-accelerating mainlobe. Since each photon in the non-diffracting, self-accelerating structure around the mainlobe carries the same OAM per photon  $\hbar k(x_s(z)y_s'(z) - y_s(z)x_s'(z))$ , the local area can be selected with some robustness (e.g., the mainlobe with several sidelobes) without affecting the measured OAM. The apertured areas are transversely synchronized with the self-accelerating mainlobes as the  $z$ -axial locations change by the delay line, monitored by CMOS1.



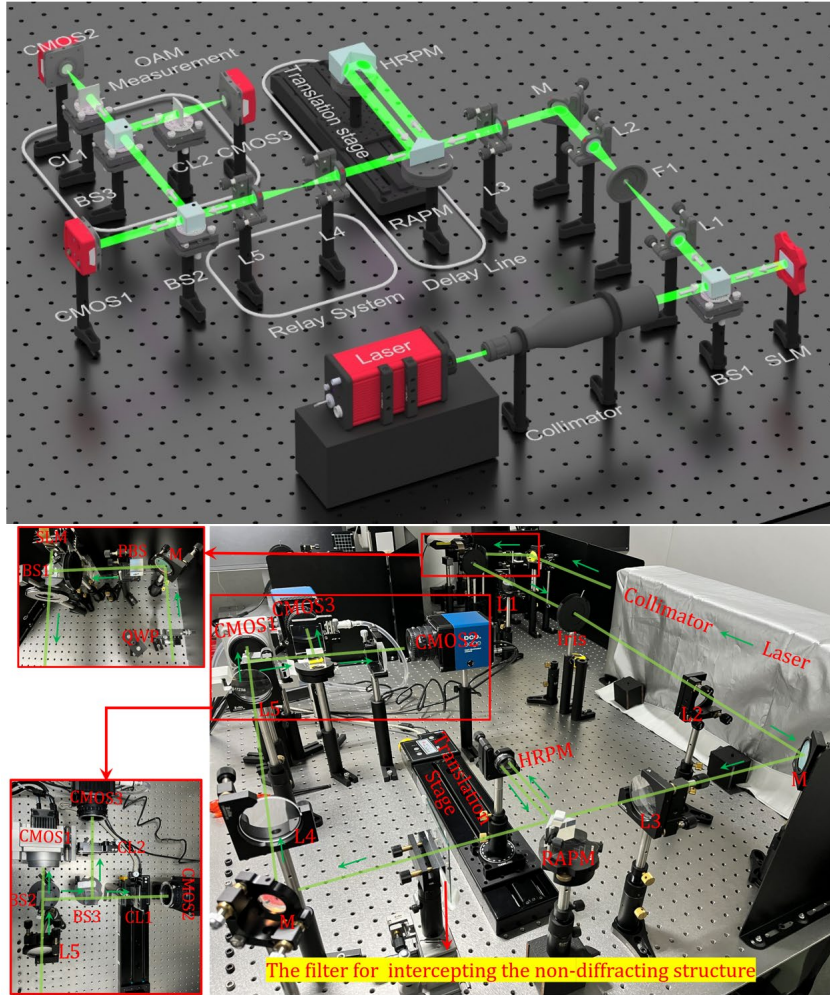


**Fig. 7.** Schematic (above) and actual (below) experimental setup for measuring the OAM of self-accelerating Bessel-like beams. BS1-3, beam splitters; SLM, phase-only spatial light modulator; L1–5, lenses; F1, filter; M, mirror; RAPM, right-angle prism mirror; HRPM, hollow roof prism mirror; CMOS1-3, complementary metal-oxide semiconductor cameras; CL1-2 cylindrical lenses. The QWP (quarter-wave plate, QWP25-532A-M from LBTEK) and PBS (polarization beam splitter) in the actual experimental setup (below) form the intensity adjustment module for the horizontally polarized beam incident on the SLM. The filter for intercepting the non-diffracting structure is fabricated with photoetched chrome hole patterns on a glass substrate, and transversely synchronized with the self-accelerating mainlobes as the z-axis locations change by the delay line, monitored by CMOS1.

**Acknowledgements** We acknowledge the support from the National Key Research and Development Program of China (2023YFA1406903) and National Natural Science Foundation of China (12374307, 12234009 and 12427808).

**Author contributions** J. D. and W.Y. conceived the project, developed the theoretical model, and designed the experiments. W.Y. and Z.Y. performed the experiments. W.Y., J.D. and H.-T.W. wrote and revised the manuscript. J.D. and H.-T.W. supervised the project. All authors contributed to discussions and manuscript preparation.

**Competing interests** The authors declare no competing interests.

**Data availability** All data that support the findings of this study are available within the article and Supplementary Information, or available from the corresponding author on reasonable request.

**Supplemental material** See Supplement information for supporting content.

## References

1. Poynting, H. J. The wave motion of a revolving shaft, and a suggestion as to the angular momentum in a beam of circularly polarised light. *Proc. R. Soc. Lond. Ser. Contain. Pap. Math. Phys. Character* **82**, 560–567 (1909).
2. Darwin, C. G. Notes on the theory of radiation. *Proc. R. Soc. Lond. Ser. Contain. Pap. Math. Phys. Character* **136**, 36–52 (1932).



3. Couillet, P., Gil, L. & Rocca, F. Optical vortices. *Opt. Commun.* **73**, 403–408 (1989).
4. Allen, L., Beijersbergen, M. W., Spreeuw, R. J. C. & Woerdman, J. P. Orbital angular momentum of light and the transformation of Laguerre-Gaussian laser modes. *Phys. Rev. A* **45**, 8185–8189 (1992).
5. Yao, A. M. & Padgett, M. J. Orbital angular momentum: origins, behavior and applications. *Adv. Opt. Photonics* **3**, 161 (2011).
6. Padgett, M. J. Orbital angular momentum 25 years on [Invited]. *Opt. Express* **25**, 11265 (2017).
7. Shen, Y. *et al.* Optical vortices 30 years on: OAM manipulation from topological charge to multiple singularities. *Light Sci. Appl.* **8**, 90 (2019).
8. Huang, S.-Y. *et al.* Spin-to-orbital angular momentum conversion via light intensity gradient. *Optica* **8**, 1231 (2021).
9. Wang, X.-L. *et al.* Optical orbital angular momentum from the curl of polarization. *Phys. Rev. Lett.* **105**, 253602 (2010).
10. Pan, Y. *et al.* Arbitrarily tunable orbital angular momentum of photons. *Sci. Rep.* **6**, 29212 (2016).
11. Lavery, M. P. J., Speirits, F. C., Barnett, S. M. & Padgett, M. J. Detection of a Spinning Object Using Light’s Orbital Angular Momentum. *Science* **341**, 537–540 (2013).
12. Ren, Z.-C. *et al.* On-demand orbital angular momentum comb from a digital laser. *Optica* **11**, 951 (2024).
13. Fang, X., Ren, H. & Gu, M. Orbital angular momentum holography for high-security encryption. *Nat. Photonics* **14**, 102–108 (2020).
14. Leach, J. *et al.* Quantum Correlations in Optical Angle–Orbital Angular Momentum Variables. *Science* **329**, 662–665 (2010).
15. Li, Y. *et al.* Two-Measurement Tomography of High-Dimensional Orbital Angular Momentum Entanglement. *Phys. Rev. Lett.* **130**, 050805 (2023).
16. Wang, J. *et al.* Terabit free-space data transmission employing orbital angular momentum multiplexing. *Nat. Photonics* **6**, 488–496 (2012).
17. Yan, W. *et al.* Iso-propagation vortices with OAM-independent size and divergence toward future faster optical communications. *Adv. Photonics* **6**, (2024).
18. Yan, W. *et al.* Energy-flow-reversing dynamics in vortex beams: OAM-independent propagation and enhanced resilience. *Optica* **11**, 531 (2024).
19. Wang, J. Advances in communications using optical vortices. *Photonics Res.* **4**, B14 (2016).
20. Courtial, J., Dholakia, K., Allen, L. & Padgett, M. J. Gaussian beams with very high orbital angular momentum. *Opt. Commun.* **144**, 210–213 (1997).
21. Berry, M. V. Optical currents. *J. Opt. Pure Appl. Opt.* **11**, 094001 (2009).
22. Berry, M. V. & Liu, W. No general relation between phase vortices and orbital angular momentum. *J. Phys. Math. Theor.* **55**, 374001 (2022).
23. Efremidis, N. K., Chen, Z., Segev, M. & Christodoulides, D. N. Airy beams and accelerating waves: an overview of recent advances. *Optica* **6**, 686 (2019).
24. Yan, W. *et al.* Non-diffracting and self-accelerating Bessel beams with on-demand tailored intensity profiles along arbitrary trajectories. *Opt. Lett.* **46**, 1494 (2021).
25. Lee, S.-H., Roichman, Y. & Grier, D. G. Optical solenoid beams. *Opt. Express* **18**, 6988 (2010).
26. Chremmos, I. D., Chen, Z., Christodoulides, D. N. & Efremidis, N. K. Bessel-like optical beams with arbitrary trajectories. *Opt. Lett.* **37**, 5003 (2012).
27. Zambirini, R. & Barnett, S. M. Quasi-Intrinsic Angular Momentum and the Measurement of Its Spectrum. *Phys. Rev. Lett.* **96**, 113901 (2006).
28. Kravtsov, Yu. A. & Orlov, Yu. I. *Causatics, Catastrophes and Wave Fields*. vol. 15 (Springer Berlin Heidelberg, Berlin, Heidelberg, 1993).
29. O’Neil, A. T., MacVicar, I., Allen, L. & Padgett, M. J. Intrinsic and Extrinsic Nature of the Orbital Angular Momentum of a Light Beam. *Phys. Rev. Lett.* **88**, 053601 (2002).
30. Bliokh, K. Y., Rodriguez-Fortuño, F. J., Nori, F. & Zayats, A. V. Spin–orbit interactions of light. *Nat. Photonics* **9**, 796–808 (2015).
31. Bekshaev, A., Bliokh, K. Y. & Soskin, M. Internal flows and energy circulation in light beams. *J. Opt.* **13**, 053001 (2011).
32. Alperin, S. N. & Siemens, M. E. Angular Momentum of Topologically Structured Darkness. *Phys. Rev. Lett.* **119**, 203902 (2017).
33. Kotlyar, V. V., Kovalev, A. A. & Porfirev, A. P. Calculation of fractional orbital angular momentum of superpositions of optical vortices by intensity moments. *Opt. Express* **27**, 11236 (2019).
34. Gibson, G. *et al.* Free-space information transfer using light beams carrying orbital angular momentum. *Opt. Express* **12**, 5448 (2004).
35. Ashkin, A. Acceleration and Trapping of Particles by Radiation Pressure. *Phys. Rev. Lett.* **24**, 156–159 (1970).
36. Yang, Y., Ren, Y.-X., Chen, M., Arita, Y. & Rosales-Guzmán, C. Optical trapping with structured light: a review. *Adv. Photonics* **3**, (2021).
37. Graham, R. & Haken, H. Laserlight - first example of a second-order phase transition far away from thermal equilibrium. *Z. Physik* **237**, 31–46 (1970).
38. Aranson, I. S. & Kramer, L. The world of the complex Ginzburg-Landau equation. *Rev. Mod. Phys.* **74**, 99–143 (2002).
39. Couillet, P., Gil, L. & Lega, J. Defect-mediated turbulence. *Phys. Rev. Lett.* **62**, 1619–1622 (1989).
40. Brambilla, M. *et al.* Transverse laser patterns. I. Phase singularity crystals. *Phys. Rev. A* **43**, 5090–5113 (1991).
41. Brambilla, M. *et al.* Transverse laser patterns. II. Variational principle for pattern selection, spatial multistability, and laser hydrodynamics. *Phys. Rev. A* **43**, 5114–5120 (1991).
42. Rosanov, N. N., Fedorov, S. V. & Shatsev, A. N. Curvilinear Motion of Multivortex Laser-Soliton Complexes with Strong and Weak Coupling. *Phys. Rev. Lett.* **95**, 053903 (2005).
43. Genevet, P., Barland, S., Giudici, M. & Tredicce, J. R. Bistable and Addressable Localized Vortices in Semiconductor Lasers. *Phys. Rev. Lett.* **104**, 223902 (2010).
44. Barland, S. *et al.* Observation of “True” Optical Vortices in a Laser System. in *Nonlinear Photonics and Novel Optical Phenomena* (eds. Chen, Z. & Morandotti, R.) vol. 170 195–205 (Springer New York, New York, NY, 2012).
45. Berry, M. V. & McDonald, K. T. Exact and geometrical optics energy trajectories in twisted beams. *J. Opt. Pure Appl. Opt.* **10**, 035005 (2008).
46. Ghosh, B. *et al.* Canonical and Poynting currents in propagation and diffraction of structured light: tutorial. *J. Opt. Soc. Am. B* **41**, 1276 (2024).
47. Allen, L., Padgett, M. J. & Babiker, M. IV The Orbital Angular Momentum of Light. in *Progress in Optics* vol. 39 291–372 (Elsevier, 1999).
48. Bliokh, K. Y., Bekshaev, A. Y., Kofman, A. G. & Nori, F. Photon trajectories, anomalous velocities and weak measurements: a classical interpretation. *New J. Phys.* **15**, 073022 (2013).
49. Kocsis, S. *et al.* Observing the Average Trajectories of Single Photons in a Two-Slit Interferometer. *Science* **332**, 1170–1173 (2011).
50. Padgett, M. J. & Allen, L. The Poynting vector in Laguerre-Gaussian laser modes. *Opt. Commun.* **121**, 36–40 (1995).
51. Madelung, E. Quantentheorie in hydrodynamischer Form. *Z. Physik.* **40**, 322–326 (1927).
52. Holland, P. R. *The Quantum Theory of Motion: An Account of the de Broglie-Bohm Causal Interpretation of Quantum Mechanics*. (Cambridge University Press, 1993). doi:10.1017/CBO9780511622687.
53. Bohm, D., Hiley, B. J. & Kaloyerou, P. N. An ontological basis for the quantum theory. *Phys. Rep.* **144**, 321–375 (1987).

54. Simpson, N. B., Dholakia, K., Allen, L., and Padgett, M. J. Mechanical equivalence of spin and orbital angular momentum of light: an optical spanner. *Opt. Lett.* **22**, 52-54 (1997).

**Supplementary Information for**  
**Vortex-free Intrinsic Orbital Angular Momentum**

**WENXIANG YAN,<sup>1,2,†</sup> ZHENG YUAN,<sup>1,2,†</sup> YUAN GAO,<sup>1,2</sup> XIAN LONG,<sup>1,2</sup> ZHI-CHENG REN,<sup>1,2</sup> XI-LIN WANG,<sup>1,2</sup> JIANPING DING,<sup>1,2,3,\*</sup> AND HUI-TIAN WANG,<sup>1,2,4</sup>**

<sup>1</sup> *National Laboratory of Solid State Microstructures and School of Physics, Nanjing University, Nanjing 210093, China*

<sup>2</sup> *Collaborative Innovation Center of Advanced Microstructures, Nanjing University, Nanjing 210093, China*

<sup>3</sup> *Collaborative Innovation Center of Solid-State Lighting and Energy-Saving Electronics, Nanjing University, Nanjing 210093, China*

<sup>4</sup> *htwang@nju.edu.cn*

<sup>†</sup> *These authors contributed equally to this work.*

<sup>\*</sup> *jpding@nju.edu.cn*

**This PDF file includes:**

Supplementary Text 1-5  
Captions for Movies S1 to S7  
References 1-20

**Other Supplementary Materials for this manuscript include the following:**

Movies S1 to S7

## Supplementary Text

### 1. Derivation of Intrinsic Vortex-free OAM in Self-Accelerating Bessel-like Beams.

**OAM theory of optical fields.** For a scalar monochromatic wave, which can be written in terms of intensity and phase as  $\psi(\mathbf{r}) = \sqrt{I(\mathbf{r})}e^{i\chi(\mathbf{r})}$ , where  $I(\mathbf{r})$  and  $\chi(\mathbf{r})$  respectively denote its intensity and phase at the coordinates  $\mathbf{r} = (x, y)$ , the transversal momentum density  $\mathbf{p}_\perp(\mathbf{r}) = I(\mathbf{r})\nabla\chi(\mathbf{r}) = (p_x(\mathbf{r}), p_y(\mathbf{r}))$  yields the global OAM per photon in the  $z$ -direction [1, 2], expressed by

$$J_z = \langle \mathbf{r} \times \mathbf{p}_\perp(\mathbf{r}) \cdot \hat{\mathbf{z}} \rangle_\perp / W = \langle xp_y(\mathbf{r}) - yp_x(\mathbf{r}) \rangle_\perp / W \quad (\text{S1})$$

where the shortened notation  $\langle \cdot \rangle_\perp = \iint dx dy$  denotes transversal integration and  $W = \langle I(\mathbf{r}) \rangle_\perp$ . In contrast to SAM, which is independent of the axis choice and thus inherently intrinsic, OAM in Eq. S1 is sensitive to the axis choice in the general case. For example, an axis shift  $\mathbf{r} \rightarrow \mathbf{r} - \mathbf{r}_d$  results in a change in OAM:  $J_z \rightarrow J_z - \langle \mathbf{r}_d \times \mathbf{p}_\perp \cdot \hat{\mathbf{z}} \rangle_\perp / W$ , reflecting both intrinsic and extrinsic contributions [3, 4]. When the initial axis is moved to the field's centroid represented by  $\mathbf{r}_c = \langle I(\mathbf{r})\mathbf{r} \rangle_\perp / W = (x_c, y_c)$ , which is the natural reference point associated with the field itself, the variation and residual of OAM are defined as the extrinsic and intrinsic constituents [2, 5, 6],

$$J_z^{\text{ext}} = \langle \mathbf{r}_c \times \mathbf{p}_\perp(\mathbf{r}) \cdot \hat{\mathbf{z}} \rangle_\perp / W = \mathbf{r}_c \times \mathbf{P}_\perp / W = (x_c P_y - y_c P_x) / W \quad (\text{S2-1})$$

$$J_z^{\text{int}} = \langle (\mathbf{r} - \mathbf{r}_c) \times \mathbf{p}_\perp(\mathbf{r}) \cdot \hat{\mathbf{z}} \rangle_\perp / W, \quad (\text{S2-2})$$

where superscripts “ext” and “int” depict the extrinsic and intrinsic contributions, respectively, and  $\mathbf{P}_\perp = \langle \mathbf{p}_\perp(\mathbf{r}) \rangle_\perp = (\langle p_x(\mathbf{r}) \rangle_\perp, \langle p_y(\mathbf{r}) \rangle_\perp) = (P_x, P_y)$  represents the transverse net momenta. Within vortex beams characterized by a transverse phase structure of  $\exp(i\ell\phi)$ , such as Bessel beams and Laguerre–Gauss beams, wherever the axis is set at any positions, the intrinsic OAM  $J_z^{\text{int}}$  equals  $\hbar\ell$  per photon regardless of the axis position, while the extrinsic OAM  $J_z^{\text{ext}}$  is always zero due to  $\mathbf{P}_\perp = 0$  [4], as established by Equations (S2-1).

**Examination of OAM in Airy beams.** The intrinsic OAM, inherent in vortex fields, contrasts sharply with the extrinsic OAM prevalent in extensive vortex-free domains. This distinction prompts a revisiting of Equation 2-1, which delineates the criteria for extrinsic OAM: a nonzero, non-collinear condition between  $\mathbf{r}_c$  and  $\mathbf{P}_\perp$ , symbolized as  $\mathbf{r}_c \times \mathbf{P}_\perp \neq 0$ . The literature [4, 7, 8] documents the elicitation and observation of extrinsic OAM through the displacement of the field's centroid ( $\mathbf{r}_c \neq 0$ ) and the disruption of the symmetrical transversal momentum density in standard vortex fields ( $\mathbf{P}_\perp \neq 0$ ), for instance, employing a soft-edged aperture to asymmetrically block part of a vortex beam or utilizing an asymmetric fractional vortex field. An encapsulation synthesizes pertinent research [3-9] by Bekshaev, Bliokh, and Soskin [2], stating, “the extrinsic OAM is associated with the geometrical optics trajectory of the beam centroid, while the intrinsic OAM describes energy flows taken to the center of the field (e.g., vortices)”. Additionally, in the context of spin-Hall effects in inhomogeneous media, it is noted that the trajectory of vortex-free self-accelerating beams aligns with the beam centroid's geometrical optics trajectory in paraxial optics.

Ehrenfest's theorem [10] and the principle of transverse net momentum conservation [11] assert that a light beam's field centroid progresses linearly and without acceleration in a vacuum. However, the local non-diffracting intensity structures—the region of interest of self-accelerating beams where the interactions with external objects predominately occur—undergo transverse acceleration during propagation [12], aligning with the geometrical optics trajectory of the local centroid. This exploration commences with an examination of the potential OAM within the local non-diffracting intensity structures of prototypical parabolic Airy beams. In Airy beams [13], the centroid,  $\mathbf{r}_c$ , and transversal net momentum,  $\mathbf{P}_\perp$ , of the local area are consistently nonzero but are mutually parallel [14], lacking tangential components because the trajectories of the centroid of Airy beams are confined solely to a meridional plane that includes the  $z$  axis, thereby precluding OAM transfer per Equation S2-1. The examination then extends to vortex-free self-accelerating beams manifesting three-

dimensional (3D) trajectories [15-17], unbounded by the two-dimensional axial constraints characteristic of Airy beams, to identify conditions fostering non-zero tangential components and, consequently, the induction of OAM.

**3D self-accelerating beams.** Based on our previous study [17], we can generate non-diffracting and self-accelerating Bessel-like beams. These beams possess local non-diffracting intensity structures (the mainlobes) that can propagate with a on-demand tailored intensity profile,  $I(z)$ , along arbitrary 3D trajectory defined by  $\mathbf{s}(z) = x_s(z)\hat{\mathbf{x}} + y_s(z)\hat{\mathbf{y}} = r_s(z)\hat{\mathbf{r}} + \varphi_s(z)\hat{\boldsymbol{\phi}}$ . The angular spectrum of such beams can be calculated using

$$A(k_x, k_y) = \mathcal{F}_z \{ \sqrt{I(z)} e^{ik_x x_s(z) + ik_y y_s(z)} e^{i\sqrt{k^2 - q^2} z} \}, \quad (\text{S3})$$

where  $(k_x, k_y, k_z)$  are the wavenumbers in Cartesian coordinates with  $k^2 = k_x^2 + k_y^2 + k_z^2$ ,  $k$  represents the free-space wavenumber, and  $q$  denotes the magnitude of the transverse component of the wavevector of the plane waves that constitute the Bessel-like beam. The subscript “z” of “ $\mathcal{F}$ ” denotes the dimension of the Fourier transform. For instance, the self-accelerating parabolic Bessel-like beam,  $\mathbf{s}(z) = 0.4 \times 10^{-3} (0, 1 - z^2 / (0.2)^2)$  with a uniform intensity distribution  $I(z) = \text{rect}[z/0.4]$ , is depicted in Fig. S1, analogous to parabolic Airy beams. The local non-diffracting structure, or the region of interest (mainlobe with several sidelobes), is indicated by the brown-dotted circle in Fig. S1(C). The centroid trajectory of the localized non-diffracting structure during propagation aligns with the self-accelerating trajectory, *i.e.*  $r_c(z) = \mathbf{s}(z)$ .

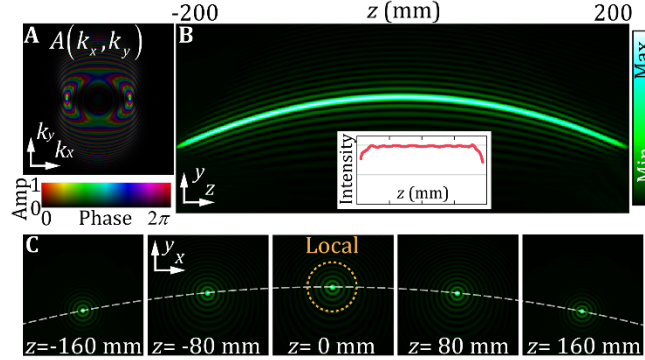


**Fig. S1.** Self-accelerating parabolic Bessel-like beam with a uniform intensity distribution along the parabolic trajectory: (A) angular spectrum distribution and (B) intensity map in the  $y$ - $z$  plane, (C) intensity maps in the five  $x$ - $y$  planes at  $z = -160$  mm,  $-80$  mm,  $0$  mm,  $80$  mm, and  $160$  mm, respectively. The brown-dotted circle roughly depicts the localized non-diffracting structure while the white dotted curve depicts the parabolic trajectory. The experimental intensity profile of the self-accelerating Bessel-like beam’s mainlobe along the trajectory is shown in the inset into (B).

**Localized transversal momentum density.** Based on the analogy between light and fluid dynamics[18], viewing the optical field as a fluid where momentum corresponds to fluid velocity, we postulate that for self-accelerating localized non-diffracting structure, the self-accelerating trajectories represent the “flow” paths of the optical system. Consequently, by solving the hydrodynamic differential equations, given by

$$d\mathbf{s}(z)/dz = \mathbf{p}_\perp / p_z \approx \mathbf{k}_\perp / k, \quad (\text{S4})$$

we predict their transversal momentum density within the local non-diffracting structure to be as described by

$$\mathbf{p}_\perp(x, y, z) = |\psi(x, y, z)|^2 k s'(z) = |\psi(x, y, z)|^2 k(x'_s(z)\hat{\mathbf{x}} + y'_s(z)\hat{\mathbf{y}}), \quad (\text{S5})$$

where  $\psi(x, y, z)$  is the complex distribution of the local non-diffracting structure and the single prime symbol denotes the first-order derivative to the variable  $z$  in parentheses. Equation (S5) is a key result of this study. As validation, we numerically calculated the transversal momentum density by [1]

$$\mathbf{p}_\perp(x, y, z) = \frac{\epsilon_0}{2\omega} \text{Im}[\psi^*(x, y, z) \cdot (\nabla)\psi(x, y, z)], \quad (\text{S6})$$



where  $\epsilon_0$  and  $\omega$  are the vacuum permittivity and circular frequency, respectively. The theoretical prediction from Eq. (S5) and the numerical calculation from Eq. (S6) show excellent agreement, as shown by three self-accelerating Bessel-like beams in Fig. S2. These beams exhibit self-accelerating trajectories, characterized by first-order (Figs. S2(A-C)) and second-order (Figs. S2(D-F)) functions in  $y$  direction, as well as cosine and sine functions in the  $x$  and  $y$  directions, respectively (Figs. S2(G-I)). This results in transversal momentum densities that are proportional to the trajectory's first derivative with respect to  $z$  (referred to as the “velocity”  $s'(z)$ ). Specially, these densities manifest as a constant (Figs. S2(C)), a linear dependence in the  $y$  direction (Figs. S2(F)), and sine and cosine dependences in the  $x$  and  $y$  direction, respectively (Fig. S2(I)). The dynamic evolution of the transverse momentum distribution are presented in Movie S1.

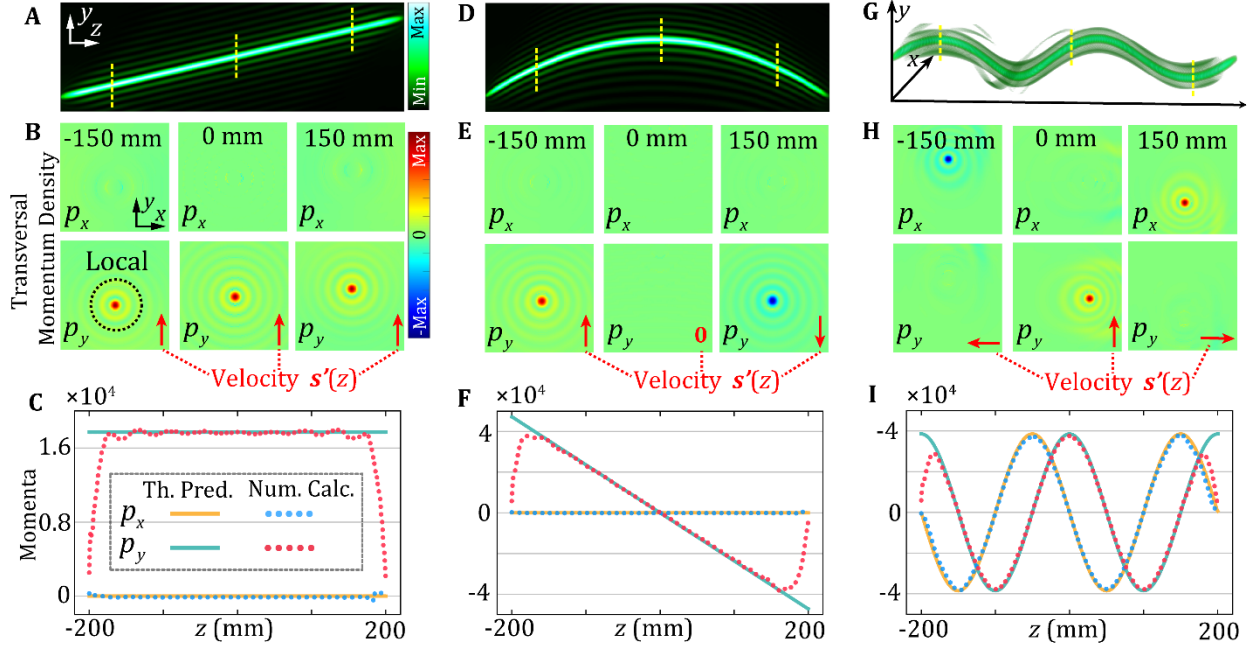


**Fig. S2.** Transversal momentum density in the local non-diffracting structure. (A) the intensity map in the  $y$ - $z$  plane of linear Bessel-like beam with  $s(z) = 0.3 \times 10^{-3}(0, z/0.2)$  and (B) the transversal momentum density at  $z = -150, 0, 150$  mm, indicated by yellow-dashed lines in (A); the black-dotted circle denotes the local non-diffracting structure and the red arrows depict the velocity vector  $s'(z)$ . (C) The self-evolution of  $p_x$  and  $p_y$  along the mainlobe, where solid curves represent theoretical predictions from Eq. (S5) and dotted curves represent numerical calculations from Eq. (S6), with the maximum intensity normalized. (D-F) and (G-I) are analogous to (A-C) but for parabolic self-acceleration  $s(z) = 0.4 \times 10^{-3}(0, 1-z^2/0.04)$  and spiral self-acceleration  $s(z) = 0.1038 \times 10^{-3}[\cos(2\pi z/0.2), \sin(2\pi z/0.2)]$ , respectively. The dynamic evolution of the transverse momentum distribution for (A-C), (D-F), and (G-I) are presented in Movie S1; the intensity profile is  $I(z) = \text{rect}(z/0.4)$ .

In the context of spirally self-accelerating Bessel-like beams, depicted in Fig. S2(G), also referred to as optical solenoid beams [15], defined by  $s(z) = R_0[\cos(\omega z), \sin(\omega z)]$  where  $R_0$  denotes the spiral radius and  $\omega z$  represents the angular velocity, we observe a unique rotational energy dynamic with the transversal momentum density  $|\psi(x, y, z)|^2 k_0 R_0 \omega z [-\sin(\omega z), \cos(\omega z)]$ . This dynamic mirrors the energy rotation observed in vortex beams, as illustrated by Allen *et al.* in Fig. 2 of [19], which is connected to the well-defined vortex-based OAM. Our analysis leads us to posit that vortex-free self-accelerating beams, particularly optical solenoid beams, harbor a well-defined OAM similar to that found in vortex beams.

**OAM in self-accelerating Bessel-like beams.** In theory, self-accelerating Bessel-like beams, similar to ideal Bessel and Airy beams, necessitate infinite power and aperture in an unbounded domain  $z \in (-\infty, \infty)$ . However, due to the finite physical apertures, these beams are confined to a limited and manageable propagation range ( $z \in (a, b)$ ). The angular spectrum of the practical self-accelerating Bessel-like beams within ( $z \in (a, b)$ ) can be expressed as [17]

$$A(k_x, k_y) = \int_a^b \sqrt{I(z)} e^{ik_x x_s(z) + ik_y y_s(z)} e^{i\sqrt{k^2 - q^2} z} e^{-ik_z z} dz. \quad (S7)$$

$I(x, y, z)$  is donated as the intensity distribution in the focal field of  $A(k_x, k_y)$ . Revisiting Eq. (S7) in a tiny  $z$ -axial range,  $(z_0, z_0 + \Delta z)$ , the angular spectrum of the self-accelerating Bessel-like beams with non-diffracting range  $(z_0, z_0 + \Delta z)$  can be expressed as

$$A_{z_0}(k_x, k_y) = \int_{z_0}^{z_0 + \Delta z} \sqrt{I(z)} e^{i(\sqrt{k^2 - q^2} z + k_x x_s(z) + k_y y_s(z))} e^{-ik_z z} dz. \quad (S8)$$

When  $\Delta z$  is tiny enough, the transversal momentum density approximately equals that at  $z_0$

$$\mathbf{p}_{\perp A_{z_0}}(x, y, z) = I_{A_{z_0}}(x, y, z) \mathbf{k} s'(z) \approx I_{A_{z_0}}(x, y, z_0) \mathbf{k} s'(z_0), \quad z \in (z_0, z_0 + \Delta z), \quad (S9)$$

where  $I_{A_{z_0}}(x, y, z)$  is the intensity distribution in the focal field of  $A_{z_0}(k_x, k_y)$ . The angular spectrum  $A(k_x, k_y)$  of a Bessel-like beam with the effective propagation range  $(a, b)$  in Eq. (S7) can be obtained by superimposing constituent angular spectrums  $A_{z_0}(k_x, k_y)$ , each controlling a tiny  $z$ -axial range  $(z_0, z_0 + \Delta z)$ :

$$A(k_x, k_y) = \sum_{z_0} A_{z_0}(k_x, k_y), \quad z_0 = a, a + \Delta z, \dots, b - \Delta z. \quad (S10)$$

The complex distribution  $E(x, y, z)$  in the focal field of  $A(k_x, k_y)$  can be obtained by coherently superimposing constituent complex distributions  $E_{A_{z_0}}(x, y, z) = \mathcal{F}_{xy} \{ A_{z_0}(k_x, k_y) e^{ik_z z} \}$

$$E(x, y, z) = \sum_{z_0} E_{A_{z_0}}(x, y, z), \quad z_0 = a, a + \Delta z, \dots, b - \Delta z. \quad (S11)$$

When  $\Delta z$  approaches 0, Equation S8 can be approximately written as

$$A_{z_0}(k_x, k_y) \approx \sqrt{I(z_0)} e^{i(\sqrt{k^2 - q^2} z_0 + k_x x_s(z_0) + k_y y_s(z_0))} e^{-ik_z z_0} \Delta z. \quad (S12)$$

The components in Eq. (S12) include: the amplitude coefficient  $\sqrt{I(z_0)}$  determines the energy of focus; the linear phase distribution  $\exp(ik_x x_s(z_0) + ik_y y_s(z_0))$  controls the transverse position of the focus at  $(x_s(z_0), y_s(z_0), 0)$ ; the quadratic phase distribution  $\exp(-ik_z z_0)$  controls the forward and backward movement of the focus at  $(x_s(z_0), y_s(z_0), z_0)$ . Therefore,  $E_{A_{z_0}}(x, y, z)$ , the focal field of  $A_{z_0}(k_x, k_y)$ , is approximately a light cone (or spherical wave) focused at  $(x_s(z_0), y_s(z_0), z_0)$  shown in Fig. S3(B). From the insets of  $x$ - $y$  maps in Fig. S3(A-B), the light cone from the angular spectrum  $A_{z_0}(k_x, k_y)$  is responsible for a single focus at  $(x_s(z_0), y_s(z_0), z_0)$  on the self-accelerating trajectory  $(x_s(z), y_s(z), z)$ , while other light cones focused at other locations ( $z \neq z_0$ ) forms the sidelobes at  $z = z_0$  by interference. For example, for the 0th-order Bessel beam (the Bessel-like beam without self-acceleration  $s(z) = 0$ ), the light cone focus at  $(0, 0, z_0)$  forms the mainlobe at  $z = z_0$ . Other light cones, focusing at  $(0, 0, z \neq z_0)$ , are divergent or convergent coaxial spherical waves at  $z = z_0$  plane and thus form the radial interference fringes (concentric rings) as sidelobes at  $z = z_0$  for the 0th-order Bessel beam. This is analogous to the geometrical mapping relationship between the transverse and longitudinal dimensions for Bessel-like beams, and can be explained by the caustic: the geometrical-optics rays of 0th-order Bessel beam are distributed on a set of coaxial cones, while those of self-accelerating Bessel-like beam are distributed on non-coaxial cones, as illustrated in Fig. 2 in the maintext.

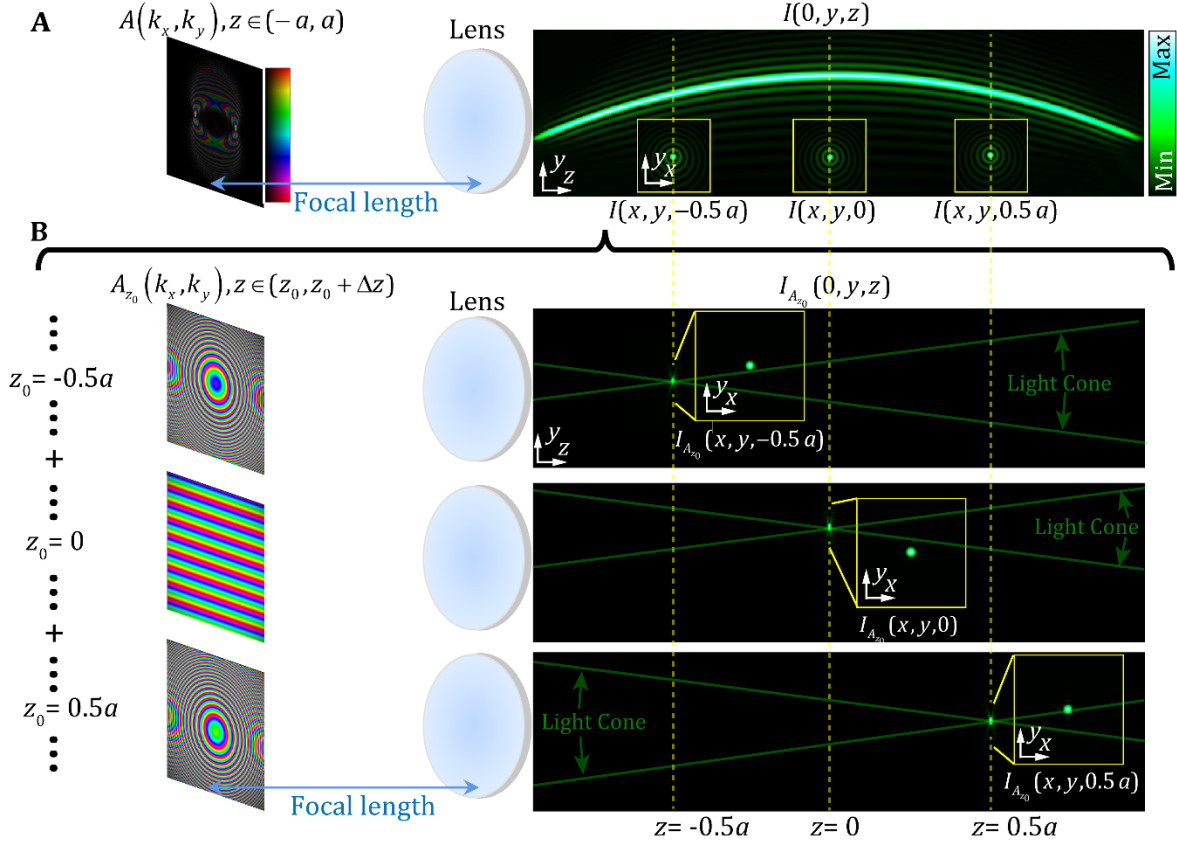


**Fig. S3.** Schematic of generating the self-accelerating Bessel-like beams with the effective propagation distance between  $(-a, a)$ . (A) illuminate the Fourier mask  $A(k_x, k_y)$  placed the front focal plane of the converging lens to generate the self-accelerating Bessel-like beam (e.g. uniform intensity along the parabolic trajectory herein) in the focal volume. The insets in the focal volume are the intensity maps in the three  $x$ - $y$  planes at  $z = -0.5a$ ,  $0$ , and  $0.5a$  (depicted by vertical yellow-dashed lines) in the focal volume, respectively. (B) illuminate the Fourier masks  $A_{z_0}(k_x, k_y)$  placed the front focal plane of the converging lens to generate the light cones focused at  $(x_s(z_0), y_s(z_0), z_0)$  while the focus of the converging lens is located at  $(0, 0, 0)$ . The upper, middle and lower rows in (B) correspond to  $z_0 = -0.5a$ ,  $0$ , and  $0.5a$  respectively and the insets are the intensity maps at  $z = z_0$  respectively in the focal volume. The green lines indicate the light cones.

For a light cone  $E_{A_{z_0}}(x, y, z)$  focused at  $(x_s(z_0), y_s(z_0), z_0)$ , the energy at any transversal plane of the light cone  $E_{A_{z_0}}(x, y, z)$  equals

$$W_{A_{z_0}} = \frac{1}{(2\pi)^2} \iint |A_{z_0}(k_x, k_y)|^2 dk_x dk_y \approx I(z_0) W_0, \quad (\text{S13-1})$$

where

$$W_0 = \frac{1}{(2\pi)^2} \iint \left| e^{i(\sqrt{k^2 - q^2} z_0 + k_x x_s(z_0) + k_y y_s(z_0))} e^{-ik_z z_0} \Delta z \right|^2 dk_x dk_y, \quad (\text{S13-2})$$

according to the Parseval's theorem. Apparently, the energy at any transversal plane of  $E_{A_{z_0}}(x, y, z)$  is proportion to  $I(z_0)$ . The total OAM at any transversal plane of the light cone  $E_{A_{z_0}}(x, y, z)$  can be expressed as those of the specific transversal  $z_0$  plane where the light cone focused at,

$$J_{A_{z_0}}^{total} = \left\langle \iint \mathbf{r} \times \mathbf{p}_{\perp A_{z_0}}(x, y, z_0) \right\rangle_{xy} = W_{A_{z_0}} k(x_s(z_0)y_s'(z_0) - y_s(z_0)x_s'(z_0)). \quad (S14)$$

The OAM per photon of the light cone  $E_{A_{z_0}}(x, y, z)$  focused at  $(x_s(z_0), y_s(z_0), z_0)$  can be written as

$$J_{A_{z_0}} = \frac{\omega J_{A_{z_0}}^{total}}{W_{A_{z_0}}} = \hbar k(x_s(z_0)y_s'(z_0) - y_s(z_0)x_s'(z_0)). \quad (S15)$$

The energy  $W_A$  and total OAM  $J_A^{total}$  at any transversal plane of the whole self-accelerating Bessel-like beams  $E(x, y, z)$  can be obtained by accumulating the energy and total OAM of each constituent light cone  $E_{A_{z_0}}(x, y, z)$ , while  $\Delta z$  approaches 0 and  $z_0$  should take over all the position between the effective propagation range  $(a, b)$ ,

$$J_A^{total} = \int_a^b J_{A_{z_0}}^{total} dz_0, W_A = \int_a^b W_{A_{z_0}} dz_0, \quad (S16)$$

and the global OAM per photon  $J_z$  of the whole self-accelerating Bessel-like beams can be expressed as

$$\begin{aligned} J_z &= \frac{\omega J_A^{total}}{W_A} = \hbar \frac{\int_a^b J_{A_{z_0}}^{total} dz_0}{\int_a^b W_{A_{z_0}} dz_0} = \hbar \frac{\int_a^b W_{A_{z_0}} J_{A_{z_0}} dz_0}{\int_a^b W_{A_{z_0}} dz_0} = \hbar \frac{\int_a^b I(z_0) J_{A_{z_0}} dz_0}{\int_a^b I(z_0) dz_0} \\ &= \hbar k \frac{\int_a^b I(z_0)(x_s(z_0)y_s'(z_0) - y_s(z_0)x_s'(z_0)) dz_0}{\int_a^b I(z_0) dz_0}. \end{aligned} \quad (S17)$$

When considering the localized non-diffracting structure (the region of interest around the mainlobe) of self-accelerating Bessel-like beams at the transversal  $z_0$  plane, owing to the light cone whose energy is focused around  $(x_s(z_0), y_s(z_0), z_0)$  forms the mainlobe while other light cones focused at others plane whose energy is diffused across whole transversal  $z_0$  plane forms the sidelobes shown in Fig. S3, the energy and total OAM in the local area around the mainlobe at transversal  $z_0$  plane in self-accelerating Bessel-like beams are dominated by the single light cone focused at  $(x_s(z_0), y_s(z_0), z_0)$  in Eq. (S15). Consequently, the local OAM per photon along the mainlobe is  $\hbar k(x_s(z)y_s'(z) - y_s(z)x_s'(z))$ .

**Intrinsic Translational Invariance of global OAM.** The global OAM may contain both intrinsic and extrinsic constituents. The extrinsic component is sensitive to the axis choice and disrupts translational invariance of optical OAM. The transverse net momenta of each light cone can be expressed as

$$\mathbf{P}_{\perp A_{z_0}} = \left\langle \mathbf{p}_{\perp A_{z_0}}(x, y, z_0) \right\rangle_{\perp} = k \mathbf{s}'(z_0) \left\langle I_{A_{z_0}}(x, y, z_0) \right\rangle_{\perp} = W_{A_{z_0}} k \mathbf{s}'(z_0). \quad (S18)$$

Owing to the conservation of transverse net momenta [11], the transverse net momenta of the self-accelerating Bessel-like beam can be obtained by accumulating all the transverse net momenta of each constituent light cone, as

$$\mathbf{P}_{\perp} = \int \mathbf{P}_{\perp A_{z_0}} dz_0 = \left\langle \left\langle I(z) k x_s'(z) \right\rangle_z \right\rangle, \left\langle \left\langle I(z) k y_s'(z) \right\rangle_z \right\rangle. \quad (S19)$$

When the transverse net momenta  $\mathbf{P}_{\perp}$  is zero, the extrinsic constituent disappears in Eq. (S2-1), rendering the global OAM purely intrinsic with translational invariance, e.g., intrinsic OAM in conventional vortex beams like high-order Bessel beams and Laguerre–Gauss beams. When  $I(z) = 1$  and  $z \in (a, b)$ , this condition of  $\mathbf{P}_{\perp} = 0$  in Eq. (S19) is reduced to

$$\mathbf{s}(a) = \mathbf{s}(b) \rightarrow (x_s(a), y_s(a)) = (x_s(b), y_s(b)). \quad (S20)$$

Equation (S20) demonstrates that the global OAM within a uniform-strength ( $I(z) = 1$ ) self-accelerating beams exhibits intrinsic translational invariance, provided the self-accelerating mainlobe ultimately resumes its original transversal position within the effective propagation range (i.e., trajectories are enclosed in the transversal position within  $\mathbf{s}(a) = \mathbf{s}(b)$  for  $z \in (a, b)$ ).

**Conclusion.** The localized OAM per photon along the self-accelerating mainlobes at  $z = z_0$  equals the OAM per photon of the constituent light cone focused at  $(x_s(z_0), y_s(z_0), z_0)$  in Eq. (S15), as

$$J_{z,local}(z_0) = J_{A_{z_0}} = \hbar k(x_s(z_0)y_s'(z_0) - y_s(z_0)x_s'(z_0)), \quad (\text{S21})$$

which is extrinsic and characterized by the self-accelerating trajectory. These local extrinsic OAM is dependent on the choice of axis and highly sensitive to positioning misalignments, thereby potentially enhancing security in optical communications and cryptography [9, 20]. This sensitivity, along with the evolving feature upon its propagation, holds promise for applications in remote positioning, sensing, and measurement. The global OAM per photon of the self-accelerating Bessel-like beams in Eq. (S17) can be rewritten as

$$J_z = \langle I(z)J_{z,local}(z) \rangle_z / \langle I(z) \rangle_z, \quad (\text{S22})$$

where the shortened notation  $\langle \psi \rangle_z = \int \psi dz$  denotes longitudinal integration. When the  $\mathbf{P}_\perp$  is zero in Eq. (S21), the global OAM of the self-accelerating Bessel-like beams, characterized by 3D self-accelerating trajectories along the mainlobes, is purely intrinsic. This novel intrinsic OAM in vortex-free self-accelerating beams introduces a third category of optical intrinsic angular momentum, complementing the established models in circularly polarized beams and vortex beams.

## 2. Vortex-free OAM in Self-accelerating Bessel-like beams with Non-uniform Intensity.

In Fig. S4, the experimental results are consistent with the theoretical predictions of Eq. (4) and Eq. (5) with different intensity profiles  $I(z)$ .

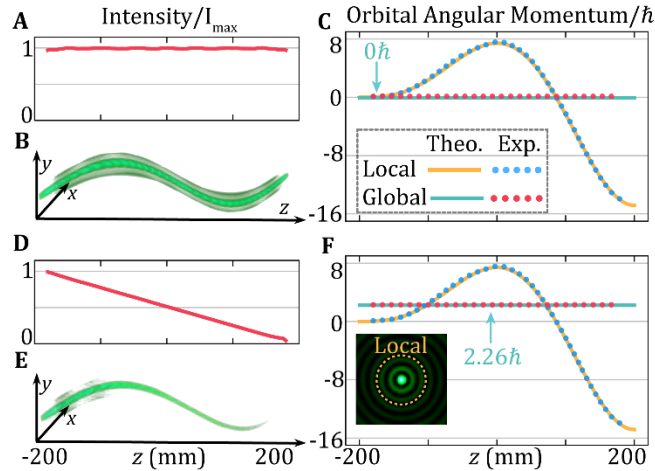


**Fig. S4.** Vortex-free OAM of self-accelerating Bessel-like beams with different intensity profiles. Panel (A) shows the intensity profile along the trajectory, while panel (B) depicts the three-dimensional intensity distribution of the entire beam with  $s(z) = 0.2[z/0.2+1, \sin(\pi z/0.2)]$  and  $I(z) = \text{rect}(z/0.4)$ . Panel (C) illustrate the local and global OAM, where the solid curves represent theoretical predictions from Eq. (4) and Eq. (5), dotted curves indicate the experimentally measured values, and the cyan value donates the theoretical global OAM. (D-F) are the same as in (A-C) but for the linearly decreased intensity profile  $I(z)=0.5(-z/0.2+1)\text{rect}(z/0.4)$ . The brown-dotted circle represents the local area apertured in the experiment shown in the inset into (F). Experimental visualization are shown in Movie S3.

## 3. Hybrid OAM in Self-accelerating Vortex Beams.

**Deriving Hybrid OAM.** The transversal wavevector components along the mainlobes of the zeroth-order self-accelerating Bessel-like beams and  $l$ th-order Bessel beams can be described as:

$$\mathbf{k}_{\perp 1}(z) = kx_s'(z)\hat{\mathbf{x}} + ky_s'(z)\hat{\mathbf{y}} = ks'(z), \quad (\text{S23-1})$$



$$\mathbf{k}_{\perp 2}(x, y, z) = \frac{1}{r} \frac{\partial(l\phi)}{\partial\phi} = \frac{l}{r} \hat{\phi} = \frac{l}{y \sin \theta + x \cos \theta} \hat{\phi}, \quad (\text{S23-2})$$

where  $\theta$  is the polar angle and  $\hat{\phi}$  is the unit vector of the azimuth direction. It is then conceivable that the transverse wavevector components along the self-accelerating annular vortex mainlobe can be formulated as:

$$\begin{aligned} \mathbf{k}_{\perp}(x, y, z) &= \mathbf{k}_{\perp 1}(z) + \mathbf{k}_{\perp 2}(x, y, z) \\ &= k_0 \mathbf{s}'(z) + \frac{l}{(y - y_s(z)) \sin \theta + (x - x_s(z)) \cos \theta} \hat{\phi} \\ &= (k_0 x_s'(z) - \frac{l}{(y - y_s(z)) \sin \theta + (x - x_s(z)) \cos \theta} \sin \theta) \hat{x} \\ &\quad + (k_0 y_s'(z) + \frac{l}{(y - y_s(z)) \sin \theta + (x - x_s(z)) \cos \theta} \cos \theta) \hat{y}, \end{aligned} \quad (\text{S24})$$

Consequently, the transversal momentum density can be expressed as

$$\mathbf{p}_{\perp}(x, y, z) = I(x, y, z) \mathbf{k}_{\perp}(x, y, z), \quad (\text{S25})$$

leading to the OAM density with both intrinsic and extrinsic components as:

$$\begin{aligned} j_z(x, y, z) &= I(x, y, z) \left[ x(ky_s'(z) + \frac{l}{(y - y_s(z)) \sin \theta + (x - x_s(z)) \cos \theta} \cos \theta \right. \\ &\quad \left. - y(kx_s'(z) - \frac{l}{(y - y_s(z)) \sin \theta + (x - x_s(z)) \cos \theta} \sin \theta) \right], \\ &= j_z^{\text{ext}}(x, y, z) + j_z^{\text{int}}(x, y, z) \end{aligned} \quad (\text{S26})$$

*where*

$$j_z^{\text{ext}}(x, y, z) = I(x, y, z) k(x_s(z)y_s'(z) - y_s(z)x_s'(z)) + \frac{Il(x, y, z)(x_s(z) \cos \theta + y_s(z) \sin \theta)}{(y - y_s(z)) \sin \theta + (x - x_s(z)) \cos \theta},$$

$$j_z^{\text{int}}(x, y, z) = I(x, y, z) [(x - x_s(z))ky_s'(z) - (y - y_s(z))kx_s'(z) + l].$$

The localized OAM per photon along the self-accelerating annular vortex mainlobe can be calculated as

$$\begin{aligned} J_{z, \text{local}}(z) &= k\hbar(x_s(z)y_s'(z) - y_s(z)x_s'(z)) + l\hbar, \\ &= J_{z, \text{local}}^{\text{ext}}(z) + J_{z, \text{local}}^{\text{int}}(z), \end{aligned} \quad (\text{S27})$$

*where*

$$J_{z, \text{local}}^{\text{ext}}(z) = k\hbar(x_s(z)y_s'(z) - y_s(z)x_s'(z)),$$

$$J_{z, \text{local}}^{\text{int}}(z) = l\hbar.$$

Finally, the global OAM for the entire self-accelerating vortex Bessel-like beam is given by:

$$\begin{aligned} J_z &= \langle I(z) J_z(z) \rangle_z / \langle I(z) \rangle_z, \\ &= \hbar k \left\langle I(z)(x_s(z)y_s'(z) - y_s(z)x_s'(z)) \right\rangle_z / \langle I(z) \rangle_z + l\hbar. \end{aligned} \quad (\text{S28})$$

Equations S24 to S28 demonstrate that the transverse momentum densities along the self-accelerating annular vortex mainlobe originate from the orbital dynamics within the beam's orbital intensity configuration (of self-acceleration) and the rotational dynamics within the optical vortex mainlobe. These two components yield both vortex-free and vortex-based OAM. When  $l = 0$ , these results are consistent with those of zeroth-order self-accelerating Bessel-like beams, and for  $l$ -th order Bessel beams with  $s(z) = 0$ , the outcomes align with standard Bessel beam characteristics.

**Validating Hybrid OAM.** Self-accelerating vortex beams, where the rotational center of an optical vortex follows a self-accelerating trajectory, are created by superimposing a vortex phase (expressed as  $\exp(il\phi)$ ) onto the angular spectrum of a zeroth-order self-accelerating Bessel-like beam in Eq. (8), as:

$$A_l(k_x, k_y) = \mathcal{F}_z \{ e^{i l \phi} \sqrt{I(z)} e^{i k_x x_s(z) + i k_y y_s(z)} e^{i \sqrt{k^2 - q^2} z} \}. \quad (\text{S29})$$

The resulting beam acquires characteristics similar to those of higher-order Bessel beams, with an annular vortex mainlobe following the predefined self-accelerating path  $\mathbf{s}(z) = [x_s(z), y_s(z)]$ , as depicted in Fig. 6 of the main text. Additionally, by allowing  $l$  to evolve as a function of propagation distance,  $l(z)$  (e.g., the piecewise function of  $z$ ), both the local vortex-free and vortex-based OAM along the self-accelerating annular vortex mainlobe can self-evolve during propagation. The expressions for local and global OAM are given by:

$$J_{z, \text{local}} = \hbar k (x_s(z) y_s'(z) - y_s(z) x_s'(z)) + l(z) \hbar, \quad (\text{S30-1})$$

$$\begin{aligned} J_z &= \langle I(z) J_z(z) \rangle_z / \langle I(z) \rangle_z, \\ &= \hbar k \langle I(z) (x_s(z) y_s'(z) - y_s(z) x_s'(z)) \rangle_z / \langle I(z) \rangle_z \\ &\quad + \hbar \langle I(z) l(z) \rangle_z / \langle I(z) \rangle_z. \end{aligned} \quad (\text{S30-2})$$

For validation, we selected the parabolic-linear trajectory  $\mathbf{s}(z) = 0.2[1 - z^2/0.04, 0.5(1 + z/0.2)]$  in Fig. 3(U) with  $I(z) = 1$  and effective propagation range  $(-200, 200)$  mm. As illustrated in Eqs. (S30) and (S31), the local and global OAM of the  $l$ -th order self-accelerating vortex beam will increase by  $l\hbar$  on the intrinsic component compared the beam with  $l = 0$ . This has been verified in Figs. S5(A-D). For the self-accelerating vortex beam with a self-evolving vortex (e.g.,  $l = 0$  for  $z < 0$  and  $l = 2$  for  $z > 0$ ) shown in Fig. S5(E), the local vortex-free and vortex-based OAM along the self-accelerating annular vortex mainlobe both evolve simultaneously, as shown in the blue-dotted curve in Fig. S5(F). The global OAM (the red-dotted curve) increase by  $\hbar$  on the intrinsic component, as indicated by Eq. (S30). For other self-accelerating vortex beams, the experimental results also matched well with the theoretical predictions from Eqs. (S27-S30).

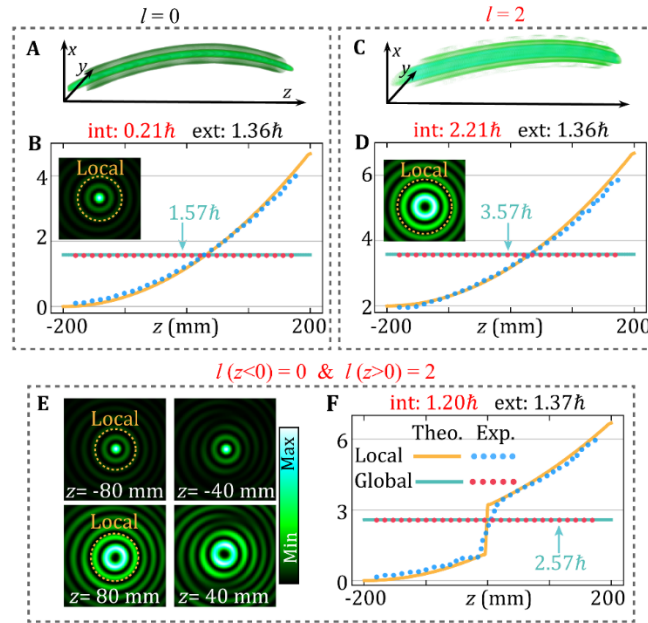


**Fig. S5.** Hybrid OAM in the self-accelerating vortex beams with  $I(z) = 1$  and effective propagation range  $(-200, 200)$  mm. (A) 3D intensity iso-surface and (B) OAM of self-accelerating beam featured by the parabolic-linear trajectory with  $\mathbf{s}(z) = 0.2[1 - z^2/200^2, 0.5(1 + z/200)]$  mm with  $l = 0$ . The brown-dotted circle in the inset of (B) represents the local area apertured in the experiment for measuring the localized OAM along the mainlobe; the top-side values mark calculated intrinsic (int) and extrinsic (ext) constituents of global OAM. Local: local OAM along the mainlobe; Global: global OAM across the transverse plane; Theo. : the theoretical predictions of Eqs. (S27-S30); Exp. : Experimental measurement. (C-D) are similar to (A-B) with the same parabolic-linear acceleration but different topological charge  $l = 2$ . (E) the local intensity maps at  $z = -80, -40, 40,$  and  $80$  mm, respectively, of the self-accelerating vortex beam with the

same trajectory but propagation-evolving topological charge  $l(z)=2\text{rect}(z/0.2-0.5)$ ; (F) Corresponding local and global OAM. Experimental visualization is in Movie S6.

#### 4. Congruence between Hydrodynamic Framework and Electrodynamics in Quantifying Optical OAM.

In the main text, we introduce a transformative hydrodynamic model that reinterprets optical fields using energy streamlines, which represent integral curves of the Poynting vector. This conceptual framework not only provides clarity on the complex rotational and orbital dynamics inherent in various optical fields but also offers a robust mechanism for quantifying the optical OAM. The process of quantifying OAM using our hydrodynamic framework involves several key steps:

1. Light is conceptualized as comprising energy streamlines, which are integral curves of the Poynting vector  $\mathbf{p}(\mathbf{R})$ .
2. These energy streamlines are visualized as 3D orbiting configurations of localized energy, following the trajectory  $\mathbf{R}(z)=\{x(z), y(z), z\}$ , by solving the hydrodynamic differential equations:  $dx(z)/dz = p_x(\mathbf{R}(z))/p_z(\mathbf{R}(z))$ ,  $dy(z)/dz = p_y(\mathbf{R}(z))/p_z(\mathbf{R}(z))$ .
3. OAM along these streamlines is quantified using a mechanical analogy, as outlined in Eq. (4) of the main text:  $J_{z,local}(z) = \mathbf{R}_\perp(z) \times (\hbar k \mathbf{R}'_\perp(z)) \cdot \hat{\mathbf{z}} = \hbar k(x(z)y'(z) - y(z)x'(z))$ , where  $\mathbf{R}_\perp(z)=\{x(z), y(z)\}$ .
4. To calculate the global OAM of the optical field, an energy-weighted average of the OAM across all streamlines originating from a selected initial plane ( $z = z_0$ ) is performed:

$$J_z = \left\langle |\psi(x, y, z_0)|^2 J_z(x, y, z_0) \right\rangle_\perp / \left\langle |\psi(x, y, z_0)|^2 \right\rangle_\perp, \quad (\text{S31})$$

where  $J_z(x, y, z_0)$  is the local OAM along the energy streamline originating from the initial plane  $z = z_0$  at  $(x, y)$ .

Through detailed analyses presented in Figs. 5 and 6, this framework has demonstrated its effectiveness across a spectrum of optical configurations, including traditional vortex beams, innovative vortex-free beams, and complex hybrid beam structures. To validate its universality, we aim to establish its congruence with the established definitions of optical OAM as framed by classical electrodynamics. Our approach shows that the hydrodynamic model does not merely replicate but also enhances the electrodynamic analysis by providing a more intuitive and physically representative depiction of the flow of angular momentum in optical fields.

Given that the trajectory  $\mathbf{R}(z)$  represents the integral curves of the Poynting vector by hydrodynamic differential equations, the local OAM  $J_{z,local}(z)$  calculated along these trajectories (using Eq. 4) can be interpreted as the OAM density distribution (per photon)  $j_z(\mathbf{R}(z))$  along that specific path  $\mathbf{R}(z)$  in the optical field:

$$J_{z,local}(z) = \mathbf{R}_\perp(z) \times (\hbar k \mathbf{R}'_\perp(z)) \cdot \hat{\mathbf{z}} = \mathbf{R}_\perp(z) \times \mathbf{p}_\perp(\mathbf{R}(z)) \cdot \hat{\mathbf{z}} = j(\mathbf{R}(z)). \quad (\text{S32})$$

When we perform an energy-weighted averaging of OAM across all trajectories emanating from a plane, we are essentially integrating the OAM density (per photon) across this plane ( $z = z_0$ ) to derive the global OAM for the entire field in electrodynamics, as illustrated in Eq. (S1):

$$\begin{aligned} J_z &= \left\langle |\psi(x, y, z_0)|^2 J_{z,local}(x, y, z_0) \right\rangle_\perp / \left\langle |\psi(x, y, z_0)|^2 \right\rangle_\perp \\ &= \left\langle |\psi(x, y, z_0)|^2 j_z(x, y, z_0) \right\rangle_\perp / \left\langle |\psi(x, y, z_0)|^2 \right\rangle_\perp \end{aligned} \quad (\text{S33})$$

Thus, the hydrodynamic approach provides a visually intuitive and physically robust framework to perceive and quantify OAM that aligns with and extends the principles of electrodynamics. This method's universality makes it applicable to any optical field, enhancing our ability to understand and manipulate the angular momentum in diverse optical settings.

**Movie S1.**

Dynamic evolution of the transverse momentum distribution for Fig. S2.

**Movie S2.**

Experimental visualizations of self-accelerating Bessel-like beams with 3D caustics in Fig. 3.

**Movie S3.**

Experimental visualizations of self-accelerating beams with different intensity profiles in Fig. S4.

**Movie S4.**

Experimental visualizations of Mechanical Transfer of Vortex-Free OAM in Optical Tweezers in Fig. 4.

**Movie S5.**

The corresponding OAM density distributions up propagation for those beams in Fig. 5.

**Movie S6.**

Experimental visualizations of self-accelerating vortex beams in Fig. S5.

**Movie S7.**

Mechanical equivalence between intrinsic vortex-free and vortex-based OAM.

**References**

1. M. V. Berry, Optical currents, *Journal of Optics A: Pure and Applied Optics* **11**, 094001 (2009).
2. A. Bekshaev, K. Y. Bliokh, M. Soskin, Internal flows and energy circulation in light beams. *Journal of Optics* **13**, 053001 (2011).
3. M. V. Berry, in *International conference on singular optics*. (International Society for Optics and Photonics, 1998), vol. 3487, pp. 6-11.
4. A. O'neil, I. MacVicar, L. Allen, M. Padgett, Intrinsic and extrinsic nature of the orbital angular momentum of a light beam. *Phys. Rev. Lett.* **88**, 053601 (2002).
5. K. Y. Bliokh, F. J. Rodríguez-Fortuño, F. Nori, A. V. Zayats, Spin-orbit interactions of light. *Nat. Photonics* **9**, 796-808 (2015).
6. C.-F. Li, Spin and orbital angular momentum of a class of nonparaxial light beams having a globally defined polarization. *Phys. Rev. A* **80**, 063814 (2009).
7. S. N. Alperin, M. E. Siemens, Angular momentum of topologically structured darkness. *Phys. Rev. Lett.* **119**, 203902 (2017).
8. S. Oemrawsingh, E. Eliel, G. Nienhuis, J. Woerdman, Intrinsic orbital angular momentum of paraxial beams with off-axis imprinted vortices. *JOSA A* **21**, 2089-2096 (2004).
9. R. Zambrini, S. M. Barnett, Quasi-intrinsic angular momentum and the measurement of its spectrum. *Phys. Rev. Lett.* **96**, 113901 (2006).
10. A. Messiah, *Quantum mechanics*. (Courier Corporation, 2014).
11. J. D. Jackson, *Classical electrodynamics*. (American Association of Physics Teachers, 1999).
12. N. K. Efremidis, Z. Chen, M. Segev, D. N. Christodoulides, Airy beams and accelerating waves: an overview of recent advances. *Optica* **6**, 686-701 (2019).
13. M. V. Berry, N. L. Balazs, Nonspreading wave packets. *American Journal of Physics* **47**, 264-267 (1979).
14. X. Weng *et al.*, Free-space creation of ultralong anti-diffracting beam with multiple energy oscillations adjusted using optical pen. *Nat. Commun.* **9**, 1-7 (2018).
15. S.-H. Lee, Y. Roichman, D. G. Grier, Optical solenoid beams. *Opt. Express* **18**, 6988-6993 (2010).
16. I. D. Chremmos, Z. Chen, D. N. Christodoulides, N. K. Efremidis, Bessel-like optical beams with arbitrary trajectories. *Opt. Lett.* **37**, 5003-5005 (2012).

17. W. Yan, Y. Gao, Z. Yuan, Z. Wang, Z.-C. Ren, X.-L. Wang, J. Ding, and H.-T. Wang, Non-diffracting and self-accelerating Bessel beams with on-demand tailored intensity profiles along arbitrary trajectories, *Opt. Lett.* **46**, 1494 (2021).
18. Graham, R. & Haken, H. Laserlight - first example of a second-order phase transition far away from thermal equilibrium. *Z. Physik* **237**, 31–46 (1970).
19. L. Allen, M. W. Beijersbergen, R. J. C. Spreeuw, and J. P. Woerdman, Orbital angular momentum of light and the transformation of Laguerre-Gaussian laser modes, *Phys. Rev. A* **45**, 8185 (1992).
20. G. Gibson, J. Courtial, M. J. Padgett, M. Vasnetsov, V. Pas'ko, S. M. Barnett, and S. Franke-Arnold, Free-space information transfer using light beams carrying orbital angular momentum, *Opt. Express* **12**, 5448 (2004).